Article

Crystal Design of Monometallic Single-Molecule Magnets Consisting of Cobalt-Aminoxyl Heterospins

Shinji Kanegawa, Satoru Karasawa, Masataka Maeyama, Motohiro Nakano, and Noboru Koga

J. Am. Chem. Soc., **2008**, 130 (10), 3079-3094 • DOI: 10.1021/ja0767579

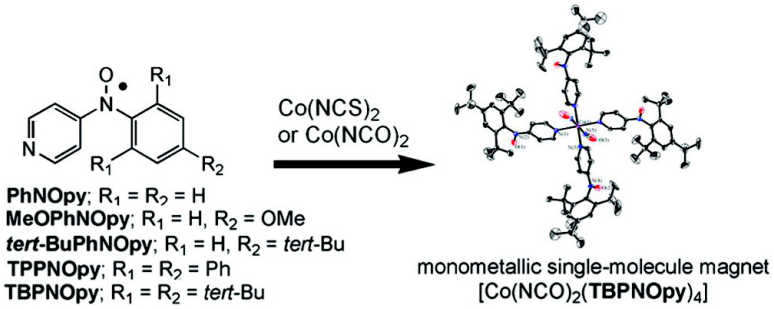

More About This Article

Additional resources and features associated with this article are available within the HTML version:

- Supporting Information
- Links to the 3 articles that cite this article, as of the time of this article download
- Access to high resolution figures
- Links to articles and content related to this article
- Copyright permission to reproduce figures and/or text from this article

View the Full Text HTML

J|A|C|S
ARTICLES
Published on Web 02/15/2008

Crystal Design of Monometallic Single-Molecule Magnets Consisting of Cobalt-Aminoxyl Heterospins

Shinji Kanegawa,[†] Satoru Karasawa,[†] Masataka Maeyama,[‡] Motohiro Nakano,[§] and Noboru Koga*,[†]

Graduate School of Pharmaceutical Sciences, Kyushu University, 3-1-1 Maidashi, Higashi-ku, Fukuoka, 812-8582 Japan, Rigaku Corporation, 3-9-12 Matsubara, Akishima, Tokyo, 196-8666 Japan, and Department of Applied Chemistry, Graduate School of Engineering, Osaka University, 2-1 Yamadaoka, Suita, Osaka, 565-0871 Japan

Received September 18, 2007; E-mail: koga@fc.phar.phyushu-u.ac.jp

Abstract: Five *N*-aryl-*N*-pyridylaminoxyls, which have no substituent (**PhNOpy**), one substituent (**MeOPhNOpy** and ***tert*-BuPhNOpy)** at the 4-position, and three substituents (**TPPNOpy** and **TBPNOpy)** at the 2, 4, and 6-positions of the phenyl ring, were prepared as new ligands for cobalt-aminoxyl heterospin systems. The 1:4 complexes, $[Co(NCS)_2(\mathbf{PhNOpy})_4]$ (**1**), $[Co(NCS)_2(\mathbf{MeOPhNOpy})_4]$ (**2**), $[Co(NCS)_2(\mathbf{\textit{tert}BuPhNOpy})_4]$ (**3**), $[Co(NCS)_2(\mathbf{TPPNOpy})_4]$ (**4**), $[Co(NCS)_2(\mathbf{TBPNOpy})_4]$ (**5a**), and $[Co(NCO)_2(\mathbf{TBPNOpy})_4]$ (**5b**), were obtained as single crystals. The molecular geometry revealed by X-ray crystallography for all complexes except **4** is a compressed octahedron. In the crystal structure of **1**, **2**, and **3**, the organic spin centers have various short contacts within 4 Å with the neighboring molecules to form 3D and 2D spin networks. On the other hand, complexes **5a** and **5b** have no significant short intermolecular contacts, indicating that they are magnetically isolated. **1** and **2** behaved as a 3D antiferromagnet with a Neel temperature, T_N, of 22 K and as a weak 3D antiferromagnet with a T_N of 2.9 K and a spin-flop field at 1.9 K, $H_{sp}(1.9)$, of 0.7 kOe, respectively. **3** was a canted 2D antiferromagnet (a weak ferromagnet) with $T_N = 4.8$ K and showed a hysteresis loop with a coercive force, H_c, of 1.3 kOe at 1.9 K. On the other hand, the trisubstituted complexes **4**, **5a**, and **5b** functioned as single-molecule magnets (SMMs). **5b** had an effective activation barrier, U_{eff}, value of 28 K in a microcrystalline state and 48 K in a frozen solution.

Single-molecule magnets (SMM)s[1−3] exhibiting slow magnetic relaxation are of interest as new functional materials, because they are a few nanometers in size and have unique quantum tunneling effects. Therefore, many metal complexes containing anisotropic metal ions[4] have been reported as SMMs over the past decade. The slow magnetic relaxation for the characteristic SMM behavior is derived from a thermal activation barrier, U, between the up spin and the down spin corresponding to $|D|S^2$; D (negative) is a zero-field splitting parameter and S is a spin quantum number. Most of the complexes reported to date except the Mn_{12} family[5] and Mn_6 complex[6a] have an effective activation barrier, U_{eff}, for the reversal of magnetism of less than 30 K (the Mn_{12} and Mn_6 complexes are $U_{eff} = 60$ and 86 K, respectively). Therefore, the construction of SMMs with large U_{eff} values become one of the challenging targets in the field of the molecule-based magnet.[6] For the construction of SMMs, we proposed the use of a heterospin system[7] consisting of the 3d spins of the metal

[†] Kyushu University.
[‡] Rigaku Corporation.
[§] Osaka University.

(1) (a) Gatteschi, D.; Sessoli, R.; Villain, J. *Molecular Nanomagnets*; Oxford University Press: New York, 2006. (b) Aromi, G.; Brechin, E. K. *Struct. Bonding* **2006**, *122*, 1−67.
(2) (a) Tasiopoulos, J.; Vinslava, A.; Wernsdorfer, W.; Abboud, K. A.; Christou, G. *Angew. Chem., Int. Ed.* **2004**, *43*, 2117−2121. (b) Murugesu, M.; Habrych, M.; Wernsdorfer, W.; Abboud, K. A.; Christou, G. *J. Am. Chem. Soc.* **2004**, *126*, 4766−4767. (c) Miyasaka, H.; Clerac, R.; Wernsdorfer, W.; Lecren, L.; Bonhomme, C.; Sugiura, K.; Yamashita, M. *Angew. Chem., Int. Ed.* **2004**, *43*, 2801−2805. (d) Brechin, E. K.; Boskovic, C.; Wenrsdorfer, W.; Yoo, J.; Yamaguchi, A.; Sanudo, E. C.; Concolino, T. R.; Rheingold, A. L.; Ishimoto, H.; Hendrickson, D. N.; Christou, G. *J. Am. Chem. Soc.* **2002**, *124*, 9710−9711. (e) Boskovic, C.; Brechin, E. K.; Streib, W. E.; Folting, K.; Bollinger, J. C.; Hendrickson, D. N.; Christou, G. *J. Am. Chem. Soc.* **2002**, *124*, 3725−3736.
(3) (a) Oshio, H.; Hoshino, N.; Ito, T.; Nakano, M. *J. Am. Chem. Soc.* **2004**, *126*, 8805−8812. (b) Andres, H.; Basler, R.; Blake, A. J.; Cadiou, C.; Chaboussant, G.; Grant, C. M.; Güdel, H. U.; Murrie, M.; Parsons, S.; Paulsen, C.; Semadini, F.; Villar, V.; Wernsdorfer, W.; Winpenny, R. E. P. *Chem.−Eur. J.* **2002**, *8*, 4867−4876. (c) Castro, S. L.; Sun, Z.; Grant, C. M.; Bollinger, J. C.; Hendrickson, D. N.; Christou, G. *J. Am. Chem. Soc.* **1998**, *120*, 2365−2375. (d) Soler, M.; Wernsdorfer, W.; Abboud, K. A.; Huffman, J. C.; Davidson, E. R.; Hendrickson, D. N.; Christou, G. *J. Am. Chem. Soc.* **2003**, *125*, 3576−3588.
(4) (a) Sun, Z. M.; Grant, C. M.; Castro, S. L.; Hendrickson, D. N.; Christou, G. *Chem. Commun.* **1998**, 721−722. (b) Gatteschi, D.; Sessoli, R.; Cornia, A. *Chem. Commun.* **2000**, 725−732. (c) Sokol, J. J.; Hee, A. G.; Long, J. R. *J. Am. Chem. Soc.* **2002**, *124*, 7656−7657. (d) Osa, S.; Kido, T.; Matsumoto, N.; Re, N.; Pochaba, A.; Mrozinski, *J. Am. Chem. Soc.* **2004**, *126*, 420−421. (e) Ishikawa, N.; Sugita, M.; Ishikawa, T.; Koshihara, S.; Kaizu, Y. *J. Am. Chem. Soc.* **2003**, *125*, 8694−8695.
(5) (a) Bian, G. O.; Kuroda-Sowa, T.; Konaka, H.; Hatano, M.; Maekawa, M.; Munakata, M.; Miyasaka, H.; Yamashita, M. *Inorg. Chem.* **2004**, *43*, 4790−4792. (b) Artus, P.; Boskovic, C.; Yoo, J.; Streib, W. E.; Brunel, L. C.; Hendrickson, D. N.; Christou, G. *Inorg. Chem.* **2001**, *40*, 4199−4210. (c) Boskovic, C.; Pink, M.; Huffman, J. C.; Hendrickson, D. N.; Christou, G. *J. Am. Chem. Soc.* **2001**, *123*, 9914−9915. (d) Chakov, N. E.; Wernsdorfer, W.; Abboud, K. A.; Hendrickson, D. N.; Christou, G. *Dalton Trans.* **2003**, 2243−2248.
(6) (a) Milios, C. J.; Vinslava, A.; Wernsdorfer, W.; Moggach, S.; Parsons, S.; Perlepes, S. P.; Christou, G.; Brechin, E. K. *J. Am. Chem. Soc.* **2007**, *129*, 2754−2755. (b) Milios, C. J.; Vinslava, A.; Wood, P. A.; Parsons, S.; Wernsdorfer, W.; Christou, G.; Perlepes, S. P.; Brechin, E. K. *J. Am. Chem. Soc.* **2007**, *129*, 8−9.

Table 1. Crystallographic Data Collection and Structural Refinement Information for **1**, **2**, and **3**

	1	2	3
empirical formula	$C_{46}H_{36}N_{10}O_4S_2Co$	$C_{54}H_{44}N_{10}O_9S_2Co$	$C_{62}H_{68}N_{10}O_4S_2Co$
formula weight	915.91	1100.06	1140.34
crystal class	monoclinic	monoclinic	monoclinic
space group	$P2_1/c$ (no. 14)	$P2_1/n$ (no. 14)	$P2_1/c$ (no. 14)
a /Å	8.9163(3)	11.2616(5)	17.0307(11)
b /Å	20.8603(7)	19.5979(7)	21.0325(13)
c /Å	11.1551(5)	23.6461(9)	10.8981(8)
α /deg	90	90	90
β /deg	91.3879(15)	90.5730(12)	129.7325(18)
γ /deg	90	90	90
V /Å^3	2074.20(14)	5218.5(4)	3002.1(3)
μ /cm^{-1}	5.740	4.761	4.101
Z	2	4	2
crystal size /mm	0.6 × 0.4 × 0.1	0.5 × 0.5 × 0.2	0.6 × 0.2 × 0.1
D_{calc} /gcm^{-3}	1.466	1.400	1.261
F(000)	946.00	2276.00	1202.00
radiation	Mo−K$_\alpha$	Mo−K$_\alpha$	Mo−K$_\alpha$
T /K	123	123	123
no. reflections measured	2930	7370	24397
no. unique reflections	632	1601	5586
no. reflections observed	3610($I > 2.00\sigma(I)$)	6150($I > 2.00\sigma(I)$)	5586(all)
no. parameters	304	704	360
R_1[a]	0.0394($I > 2.00\sigma(I)$)	0.0631 ($I > 2.00\sigma(I)$)	0.0580 ($I > 2.00\sigma(I)$)
wR_2[a]	0.1091 ($I > 2.00\sigma(I)$)	0.1603($I > 2.00\sigma(I)$)	0.1720 (all reflections)
GOF	1.000	1.005	1.077

[a] $R_1 = \Sigma\ ||F_0| - |F_c||/\ \Sigma\ |F_0|$; $wR_2 = \{\Sigma\ w(F_0^2 - F_c^2)^2/\ \Sigma\ w(F_0^2)^2\}^{1/2}$.

Table 2. Crystallographic Data Collection and Structural Refinement Information for **5a**, **5b**, **TPPNOpy**, and **TBPNOpy**

	5a	5b	TPPNOpy	TBPNOpy
empirical formula	$C_{102}H_{152}N_{10}O_6S_2Co$	$C_{102}H_{152}N_{10}O_8Co$	$C_{29}H_{21}N_2O$	$C_{23}H_{33}N_2O$
formula weight	1737.44	1896.80	413.50	353.53
crystal class	triclinic	triclinic	monoclinic	monoclinic
space group	$P\bar{1}$ (no. 2)	$P\bar{1}$ (no. 2)	$P2_1/c$ (no. 14)	$P2_1/c$ (no. 14)
a /Å	10.1796(8)	10.3678(5)	18.2162(6)	9.9900(4)
b /Å	12.5417(9)	12.4883(7)	10.8471(5)	19.4317(8)
c /Å	20.2773(15)	20.1384(8)	22.0773(8)	11.8283(5)
α /deg	74.475(2)	75.1828(14)	90	90
β /deg	83.843(2)	83.0490(11)	98.4008(10)	116.3259(15)
γ /deg	83.886(2)	84.7460(16)	90	90
V /Å^3	2483.1(3)	2497.2(2)	4315.3(3)	2058.00(15)
μ /cm^{-1}	2.712	2.296	0.775	0.693
Z	1	1	8	4
crystal size /mm	0.6 × 0.2 × 0.1	0.7 × 0.6 × 0.6	0.5 × 0.3 × 0.3	0.7 × 0.6 × 0.4
D_{calc} /gcm^{-3}	1.162	1.134	1.273	1.141
F(000)	941.00	925.00	1736.00	772.00
radiation	Mo−K$_\alpha$	Mo−K$_\alpha$	Mo−K$_\alpha$	Mo−K$_\alpha$
T /K	123	123	123	123
no. reflections measured	3644	33675	9705	2908
no. unique reflections	1535	9147	1321	631
no. reflections observed	4080($I > 3.00\sigma(I)$)	9147($I > 3.00\sigma(I)$)	3803($I > 2.00\sigma(I)$)	2728($I > 3.00\sigma(I)$)
no. parameters	623	549	619	268
R_1[a]	0.0863($I > 3.00\sigma(I)$)	0.0627($I > 2.00\sigma(I)$)	0.0525($I > 2.00\sigma(I)$)	0.0924($I > 3.00\sigma(I)$)
wR_2[a]	0.2415($I > 3.00\sigma(I)$)	0.2011 (all refrections)	0.0971($I > 2.00\sigma(I)$)	0.2685($I > 3.00\sigma(I)$)
GOF	0.955	1.140	1.004	1.001

[a] $R_1 = \Sigma\ ||F_0| - |F_c||/\ \Sigma\ |F_0|$; $wR_2 = \{\Sigma\ w(F_0^2 - F_c^2)^2/\ \Sigma\ w(F_0^2)^2\}^{1/2}$.

ion and the 2p spins of the unpaired electrons of the organic radicals coupled magnetically through a linker. According to our strategy, the 1:4 complexes of $Co(NCS)_2$ with (4-pyridyl)-phenylcarbene, **C1py**, and $Co(NCO)_2$ with *N*-*tert*-butyl-*N*-4-pyridylaminoxyl, **4NOpy**, were prepared and showed SMM behavior with U_{eff} = 89 and 50 K, respectively, in frozen solution.[8,9] In a series of 1:4 complexes, $[Co(X)_2(\mathbf{4NOpy})_4]$ (X = Br$^-$, NCS$^-$, and NCO$^-$), furthermore, SMM behavior was found to be controlled by the axial ligand X; the U_{eff} values increased in the order of Br$^-$, NCS$^-$, and NCO$^-$.[10] However, SMM magnetic behavior was observed in frozen solution but not in a crystalline state. The absence of a SMM magnetic behavior in the crystalline state is mainly due to the strong intermolecular interaction. In the 1:4 complexes of $[Co(X)_2$-

(7) (a) Karasawa, S.; Kumada, H.; Koga, N.; Iwamura, H. *J. Am. Chem. Soc.* **2001**, *123*, 9685−9686. (b) Karasawa, S.; Koga, N. *Polyhedron* **2003**, *22*, 1877−1882. (c) Morikawa, H.; Karasawa, S.; Koga, N. *Appl. Magn. Reson.* **2003**, *23*, 507−515. (d) Karasawa, S.; Koga, N. *Polyhedron* **2001**, *20*, 1387−1389. (e) Morikawa, H.; Imamura, F.; Tsurukami, Y.; Itoh, T.; Kumada, H.; Karasawa, S.; Koga, N.; Iwamura, H. *J. Mater. Chem.* **2001**, *11*, 493−502.

(8) (a) Karasawa, S.; Zhou, G.; Morikawa, H.; Koga, N. *J. Am. Chem. Soc.* **2003**, *125*, 13676−13677. (b) Tobinaga, H.; Suehiro, M.; Ito, T.; Zhou, G.; Karasawa, S.; Koga, N. *Polyhedron*, **2007**, *26*, 1905−1911.

(9) Kanegawa, S.; Karasawa, S.; Nakano, M.; Koga, N. *Chem. Commun.* **2004**, 1750−1751.

(10) Kanegawa, S.; Karasawa, S.; Nakano, M.; Koga, N. *Bull. Chem. Soc. Jpn.* **2006**, *79*, 1372−1382.

(**4NOpy**)$_4$], the spin centers of aminoxyl are located at the periphery of the complex and easily come close to those in the neighboring complex molecules. Actually, short contacts (<4 Å) between the aminoxyl centers and between the aminoxyl center and the pyridine ligands belonging to the neighboring molecules are often observed in the crystal structure of [Co(X)$_2$(**4NOpy**)$_4$] and many other heterospin complexes. For the observation of SMM behavior, therefore, we are compelled to use frozen solutions to avoid intermolecular interactions.

Although intermolecular magnetic interaction in the crystalline state is undesirable for SMMs, the interaction can be regarded as the formation of a new spin network. This means that a discrete cobalt(II) complex in the crystalline state is expected to form a low-dimensional spin network and show unique magnetic behavior affected by the magnetic anisotropy of the cobalt(II) ion.[11] Indeed, the crystalline samples of [Co(X)$_2$(**4NOpy**)$_4$] (X = NCS$^-$ and NCO$^-$,[10]) and [CoCl$_2$(**4NOPyOMe**)$_2$],[12] showed anisotropic magnetic behavior. The former were anitiferromagnet with T_N = 15 and 4.5 K, respectively, and the latter showed anisotropic 2D magnetic behavior with a magnetic phase transition of T_c = 2.14 K and a glass-like magnetic behavior below T_c.

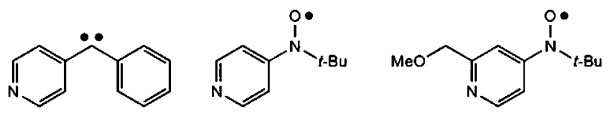

C1py 4NOpy 4NOpy-OMe

To understand the correlation between the magnetism and the crystal structure in the heterospin cobalt complex, this time we considered controlling the crystal lattice of the 1:4 complex by changing systematically the size of the substituents on the aminoxyl-pyridine ligands and aimed at the observation of the monometallic SMM in the crystalline state. Until now, **4NOpy** has been used as a metal ligand carrying an organic spin source in our heterospin SMM. However, it is inadequate for this study. Based on previous studies of the heterospin complexes, an *N*-phenyl-*N*-pyridylaminoxyl, **PhNOpy**, in which the *tert*-butyl group of **4NOpy** was replaced with a phenyl ring, was selected as a framework of the new ligand for introducing different-sized substituent(s). In this study, *N*-aryl-*N*-pyridylaminoxyls (**MeOPhNOpy**, ***tert*-BuPhNOpy**, **TPPNOpy**, and **TBPNOpy**) having one or three substituents (−OMe, -*tert*-Bu, and −Ph) on the phenyl ring were prepared in addition to **PhNOpy** and the 1:4 complexes of Co(X)$_2$ (X = NCS$^-$ and NCO$^-$) with *N*-aryl-*N*-pyridylaminoxyls, [Co(NCS)$_2$(**PhNOpy**)$_4$] (**1**), [Co(NCS)$_2$(**MeOPhNOpy**)$_4$] (**2**), [Co(NCS)$_2$(***tert*-BuPhNOpy**)$_4$] (**3**), [Co(NCS)$_2$(**TPPNOpy**)$_4$] (**4**), [Co(NCS)$_2$(**TBPNOpy**)$_4$] (**5a**), and [Co(NCO)$_2$(**TBPNOpy**)$_4$] (**5b**), were obtained as crystals. The crystal structures of the 1:4 cobalt complexes were characterized by X-ray crystallography and their magnetic properties in the crystalline state were investigated. Finally, we found the 1:4 complexes, **4**, **5a**, and **5b**, showing SMM behavior in the crystalline state and confirmed that they exhibit similar SMM behavior in frozen solution.

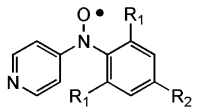

PhNOpy; R$_1$ = R$_2$ = H
MeOPhNOpy; R$_1$ = H, R$_2$ = OMe
***tert*-BuPhNOpy**; R$_1$ = H, R$_2$ = *tert*-Bu
TPPNOpy; R$_1$ = R$_2$ = Ph
TBPNOpy; R$_1$ = R$_2$ = *tert*-Bu

Experimental Section

General Methods. Infrared spectra were recorded on a JASCO 420 FT-IR spectrometer. Vis-Nir spectra were recorded on a JASCO V570 spectrometer. ^{1}H NMR spectra were measured on a JEOL 270 Fourier transform spectrometer and a Varian UNITY INOVA (400 MHz) using $CDCl_3$ (or DMSO-d_6) as solvent and referenced to TMS. EPR spectra were recorded on a Bruker Biospin EMX EPR X-band (9.4 GHz) spectrometer. FAB mass spectra (FAB MS) were recorded on a JEOL JMS-SX102 spectrometer. Melting points were obtained with a MEL-TEMP heating block and are uncorrected. Elemental analyses were performed in the Analytical Center of the Faculty of Science in Kyushu University.

X-Ray Molecular and Crystal Structure Analyses. Crystallographic data and experimental details are summarized in Table 1 for **1**, **2**, and **3** and in Table 2 for **5a** and **5b** together with free aminoxyls, **TPPNOpy** and **TBPNOpy**. Suitable single crystals were glued onto a glass fiber using epoxy resin. All X-ray data were collected on a Rigaku Raxis-Rapid diffractometer with graphite monochromated Mo-K$_\alpha$ radiation (λ = 0.71069 Å). Reflections were collected at 123 ± 1 K. The molecular structures were solved by direct methods (SIR program) and expanded using Fourier techniques (DIRDIF94). The refinements were converged using the full-matrix least-squares method from the Crystal Structure software package[13] to give the $P2_1/c$ (no. 14) for **1**, **3**, **TPPNOpy**, and **TBPNOpy**, $P2_1/n$ (no. 14) for **2**, and $P\bar{1}$ (no. 2) for **5a** and **5b**. All non-hydrogen atoms were refined anisotropically, hydrogen atoms were included at standard positions (C−H = 0.96 Å, C−C−H = 120 °) and refined isotropically using a rigid model. Crystallographic data for the structure reported in this paper have been deposited with the Cambridge Crystallographic Data Center as supplementary publications no. CCDC-626043, -626044, -652128, -626045, -652127, -626041, and -626042 for **1**, **2**, **3**, **5a**, **5b**, **TPPNOpy**, and **TBPNOpy**, respectively.

SQUID Measurements. Direct current (dc) and alternating current (ac) magnetic susceptibility data were obtained on Quantum Design MPMS5S and MPMS2 SQUID magneto/susceptometer, respectively, and corrected for the magnetization of the sample holder and capsule and for diamagnetic contributions to the samples, which were estimated from Pascal's constants.[14] A pulverized sample was prepared by grinding the complex crystal to powder and restrained by eicosane in a sample capsule to avoid partial reorientation of the crystal during the measurement. For the magnetic measurement of a direction-arranged sample of **5b**, a single crystal (1.0 × 0.8 × 0.4 mm^3) was selected and used. The orientation of the crystal's axis was determined by X-ray analysis, and then the crystal was arranged on a sample holder. Solution samples (5 or 10 mM) were prepared as follows: the crystal of the complex was dissolved in toluene, and 150 μL of solution sample was placed in a sample capsule. Dc magnetic susceptibility was measured by a sequence of ZFCM (zero field cooled magnetization), FCM (field cooled magnetization), and RM (remnant magnetization) at a dc field

(11) (a) Murrie, M.; Teat, S. J.; Stoeckli-Evans, H.; Güdel, H.-U. *Angew. Chem., Int. Ed.* **2003**, *42*, 4653−4656. (b) Galan-Mascaros, J. R.; Dunbar, K. R. *Angew. Chem., Int. Ed.* **2003**, *42*, 2289−2293. (c) Yang, E. C.; Hendrickson, D. N.; Wernsdorfer, W.; Nakano, M.; Zakharov, L. N.; Sommer, R. D.; Rheingold, A. L.; Ledezma-Gaeraud, M.; Christou, G. *J. Appl. Phys.* **2002**, *91*, 7382−7384. (d) Caneschi, A.; Gatteschi, D.; Lalioti, N.; Sessoli, R.; Sorace, L.; Tangoulis, V.; Vindigni, A. *Chem.−Eur. J.* **2002**, *8*, 286−292.
(12) Zhu, Z.; Karasawa, S.; Koga, N. *Inorg. Chem.* **2005**, *44*, 6004−6011.
(13) *SIR 92*: Altomare, A.; Burla, M. C.; Camalli, M.; Cascarano, M.; Giacovazzo, C.; Guagliardi, A.; Polidori, G. *J. Appl. Cryst.* **1994**, *27*, 435. (b) Beurskens, P. T.; Admiraal, G.; Beurskens, G.; Bosman, W. P.; de Gelder, R.; Israel, R.; Smits, J. M. M. *DIRDIF99*; The DIRDIF-99 program system, Technical Report of the Crystallography Laboratory; University of Nijmegen: The Netherlands, 1994. (c) *Crystal Structure 3.5.1*; Crystal Structure Analysis Package; Rigaku and Rigaku/MSC: The Woodlands, TX, 2000−2003.
(14) Kahn, O. *Molecular Magnetism*; Wiley-VCH Publishers: Weinheim, 1993.

of 4.7 Oe. Ac magnetic susceptibility measurements were carried out with a 3.9 Oe oscillating field and a zero dc field at a frequency of 1−997 Hz.

Materials. Diethyl ether and toluene were distilled from sodium benzophenone ketyl. Dichloromethane was distilled under high-purity N_2 after drying with calcium hydride. The nitroso derivatives, nitrosobenzene,[15a] 4-methoxynitrosobenzene, 4-*tert*-butylnitrosobenzene, 2,4,6-triphenylnitrosobenzene,[15b] and 2,4,6-tri-*tert*-butylnitrosobenzene[15c] were prepared by procedures reported in the literature. $Co(NO_3)_2 \cdot 6H_2O$, KNCO, and $Co(NCS)_2$ were purchased and used without purification.

4-{*N*-Phenyl-*N*-hydroxylamino}pyridine, **PhNOHpy.** A 1.58 M solution of *n*-butyllithium (7.6 mL) in *n*-hexane was added at −78 °C to a solution of 4-bromopyridine (1.57 g, 10.0 mmol) in 100 mL of anhydrous diethyl ether. After 30 min of stirring, a solution of nitrosobenzene (1.51 g, 14.0 mmol) in dry diethyl ether (50 mL) was added dropwise. The reaction mixture was stirred for 15 min at −78 °C and allowed to warm slowly to room temperature overnight. The reaction was quenched with saturated aqueous ammonium chloride. The resulting light-brown precipitate was collected by filtration and washed with diethyl ether/*n*-hexane to give the hydroxylamine **PhNOHpy** (0.85 g, 48.8% yield) as a white solid: mp 158−160 °C, ^{1}H NMR (270 MHz, DMSO-d_6) δ 8.24 (d, J = 6.01 Hz, 2H), 7.45 (t, J = 7.73 Hz, 2H), 7.36 (d, J = 6.71 Hz, 2H), 7.26 (t, J = 7.38 Hz, 1H), 6.87 (d, J = 6.71 Hz, 2H), FAB MS (in *m*-NBA matrix), 187.2 (M+1), Anal. Calcd for $C_{11}H_{10}N_2O$: C 70.95, H 5.41, N 15.04%; found: C 70.88, H 5.41, N 15.03%.

4-{*N*-(4-Methoxyphenyl)-*N*-hydroxylamino}pyridine, **MeOPhNOHpy.** This was prepared in a manner similar to **PhNOHpy** using 4-nitrosoanisole in place of nitrosobenzene. The hydroxylamine **MeOPhNOHpy** (1.25 g, 57.8% yield) was obtained as a white solid: mp (dec) 143−145 °C, ^{1}H NMR (270 MHz, DMSO-d_6) δ 8.19 (d, J = 6.05 Hz, 2H), 7.27 (d, J = 8.73 Hz, 2H), 7.01 (d, J = 8.73 Hz, 2H), 6.73 (d, J = 6.04 Hz, 2H), 3.79 (s, 3H), FAB MAS (in *m*-NBA matrix) 217.4 (M+1), Anal. Calcd. for $C_{12}H_{12}N_2O_2$: C 66.65, H 5.59, N 12.96%; found: C 66.93, H 5.61, N 12.99%.

4-{*N*-(4-*tert*-Butylphenyl)-*N*-hydroxylamino}pyridine, ***tert*-BuPhNOHpy.** This was prepared in a manner similar to **PhNOHpy** using 4-*tert*-butylnitrosobenzene in place of nitrosobenzene. The hydroxylamine (0.98 g, 40.6% yield) was obtained as a white solid: mp (dec) 170−172 °C, ^{1}H NMR (270 MHz, DMSO-d_6) δ 8.22 (d, J = 6.04 Hz, 2H), 7.47 (d, J = 8.06 Hz, 2H), 7.27 (d, J = 8.72 Hz, 2H), 6.83 (*d*, J = 6.04 Hz, 2H), 1.30 (*s*, 9H), FAB MS (in *m*-NBA matrix), 243.3 (M+1), Anal. Calcd for $C_{15}H_{18}N_2O$: C 74.35, H 7.49, N 11.56%; found: C 74.14, H 7.50, N 11.57%.

4-{*N*-(2,4,6-Tri-*tert*-butylphenyl)-*N*-hydroxylamino}pyridine, TBPNOHpy. A mixture of a 1.58 M solution of *n*-butyllithium (38 mL) in *n*-hexane and TMEDA (6.96 g, 60 mmol) was stirred for 5 min in a nitrogen atmosphere. The solution was cooled to −78 °C and diethyl ether (300 mL) was added. A solution of 4-bromopyridine (7.9 g, 50 mmol) in diethyl ether (200 mL) was added dropwise. Next a solution of 2, 4, 6-tri-*tert*-butylnitrosobenzene (13.8 g, 50 mmol) in diethyl ether (100 mL) was added immediately. The reaction mixture was stirred for 1 h at −78 °C and allowed to warm slowly to room temperature overnight. The reaction was quenched with saturated aqueous ammonium chloride. The resulting precipitate was collected by filtration and washed with diethyl ether/*n*-hexane to give hydroxylamine (1.12 g, 6.3% yield) as a white solid: mp (dec) 233−235 °C, ^{1}H NMR (270 MHz, DMSO-d_6) δ 9.39 (br, 1H), 8.16 (br, 1H), 7.89 (br, 1H), 7.52 (*s*, 2H), 6.76 (br, 1H), 5.50 (br, 1H), 1.32 (*s*, 9H), 1.27 (*s*, 18H); FAB MS (in *m*-NBA matrix), 355.4 (M+1); Anal. Calcd for $C_{23}H_{34}N_2O$: C 77.92, H 9.67 N 7.90%; found: C 78.01, H 9.62, N 7.98%.,

4-{*N*-(2,4,6-Triphenylphenyl)-*N*-hydroxylamino}pyridine, TPPNOHpy. This was prepared in a manner similar to **PhNOHpy** using 2,4,6-triphenylnitrosobenzene in place of nitrosobenzene. The dark-colored oil was chromatographed on silica gel with chloroform/methanol (8/1) as eluent to give the hydroxylamine (0.81 g, 6.5% yield) as a white solid: mp (dec) 243−244 °C, ^{1}H NMR (400 MHz, DMSO-d_6) δ 9.80 (br, 1H), 7.88 (d, J = 5.80 Hz, 2H), 7.83 (d, J = 8.61 Hz, 2H), 7.68 (*s*, 2H), 7.51−7.41 (m, 7H), 7.32−7.26 (m, 6H) 6.29 (br, 2H), FAB MS (in *m*-NBA matrix), 415.3 (M+1); Anal. Calcd for $C_{29}H_{22}N_2O$: C 84.03, H 5.35, N 6.76%; found: C 83.25, H 5.46, N 6.69%.

4-(*N*-Phenyl-*N*-oxylamino)pyridine, **PhNOpy.** Ag_2O (187 mg, 0.81 mmol) was added to a solution of **PhNOHpy** (100 mg, 0.54 mmol) in diethyl ether (20 mL) at room temperature. The suspension was stirred for 20 min and filtered. *n*-Hexane (30 mL) was added to the filtrate. The solution was slowly evaporated, and a resulting precipitate was collected by filtration. **PhNOpy** (71 mg, 71.4% yield) was obtained as a red powder: mp (dec) 68 °C; ESR (CH_2Cl_2) a_N = 9.3 G. FAB MS (in *m*-NBA matrix), 186.2 (M+1), Anal. Calcd for $C_{11}H_9N_2O$: C 71.34, H 4.90, N 15.13%; found: C 71.35, H 4.95, N 15.02%.

4-{*N*-(4-Methoxyphenyl)-*N*-oxylamino}pyridine, **MeOPhNOpy.** This was prepared in a manner similar to **PhNOpy** using **MeOPhNOHpy** (100 mg, 0.46 mmol). **MeOPhNOpy** (63 mg, 63.2% yield) was obtained as a red powder: mp (dec) 112 °C; ESR (CH_2Cl_2) a_N = 9.4 G. FAB MS (in *m*-NBA matrix), 216.2 (M+1), Anal. Calcd for $C_{12}H_{11}N_2O_2$: C 66.97, H 5.15, N 13.02%; found: C 66.95, H 5.19, N 13.01%.

4-{*N*-(4-*tert*-Butylphenyl)-*N*-oxylamino}pyridine, *tert*-BuPhNOpy. This was prepared in a manner similar to **PhNOpy** using ***tert*-BuPhNOHpy** (100 mg, 0.41 mmol). ***tert*-BuPhNOpy** (74 mg, 74.3% yield) was obtained as a red powder: mp (dec) 80 °C; ESR (CH_2Cl_2) a_N = 9.4 G. FAB MS (in *m*-NBA matrix), 242.2 (M+1), Anal. Calcd for $C_{15}H_{17}N_2O$: C 74.66, H 7.10, N 11.61%; found: C 74.54, H 7.25, N 11.59%.

4-{*N*-(2,4,6-*tert*-Butylphenyl)-*N*-oxylamino}pyridine, **TBPNOpy.** This was prepared in a manner similar to **PhNOpy** using **TBPNOHpy**. **TBPNOpy** (76 mg, 76.2% yield) was obtained as a yellow crystal: mp (dec) 144 °C; ESR (CH_2Cl_2) a_N = 9.2 G. FAB MS (in *m*-NBA matrix), 354.4 (M+1), Anal. Calcd for $C_{23}H_{33}N_2O$: C 78.14, H 9.41, N 7.92%; found: C 78.03, H 9.49, N 7.83%.

4-{*N*-(2,4,6-Triphenylphenyl)-*N*-oxylamino}pyridine, **TPPNOpy.** This was prepared in a manner similar to **PhNOpy** using **TPPNOHpy**. **TPPNOpy** (84 mg, 84.2% yield) was obtained as a red crystal: mp (dec) 202 °C; ESR (CH_2Cl_2) a_N = 9.2 G; FAB MS (in *m*-NBA matrix), 414.3 (M+1); Anal. Calcd for $C_{29}H_{21}N_2O \cdot 3/7CH_2Cl_2$: C 78.57, H 4.90, N 6.23%; found: C 78.52, H 4.91, N 6.29%.

Tetrakis{4-(*N*-Phenyl-*N*-oxylamino)pyridine}di(thiocyanato-*N*)-cobalt(II), [Co(NCS)$_2$(PhNOpy)$_4$] (1). A solution of $Co(NCS)_2$ (35.5 mg, 0.20 mmol) in EtOH (0.5 mL) and a solution of **PhNOpy** (150 mg, 0.81 mmol) in dichloromethane (30 mL) were mixed. *n*-Hexane (15 mL) was added to the mixture, and then the volume of the solution was reduced to ca. 30 mL on a rotary evaporator. The resulting precipitates were removed by filtration, and the solution was kept at −30 °C. The complex **1** was obtained as dark-red platelet crystals (123 mg): mp (dec) 124−126 °C,IR (KBr pellet) ν = 2074 cm^{-1} (NCS); Anal. Calcd for $C_{46}H_{36}N_{10}O_4S_2Co \cdot 1/6CH_2Cl_2$: C 59.79, H 3.94, N 15.12%; found: C 59.80, H 4.15, N 14.90%.

Tetrakis[4-{*N*-(4-Methoxyphenyl)-*N*-oxylamino}pyridine]di-(thiocyanato-*N*)cobalt(II), [Co(NCS)$_2$(MeOPhNOpy)$_4$] (2). This was prepared in a manner similar to the procedure for **1** by using **MeOPhNOpy**. The complex **2** was obtained as dark-red brick-like crystals (142 mg): mp (dec) 182−184 °C,IR (KBr pellet) ν = 2059 cm^{-1} (NCS); Anal. Calcd for $C_{50}H_{44}N_{10}O_8S_2Co \cdot 3/4Et_2O$: C 58.32, H 4.76, N 12.83%; found: C 58.57, H 4.76, N 12.99%.

Tetrakis[4-{*N*-(4-*tert*-Butylphenyl)-*N*-oxylamino}pyridine]di-(thiocyanato-*N*)cobalt(II), [Co(NCS)$_2$(*tert*-BuPhNOpy)$_4$] (3). This

(15) (a) Porta, F.; Prati, L. *J. Mol. Catal.* **2000**, *157*, 123−129. (b) Kanaya, S.; Kozaki, M.; Shiomi, D.; Sato, K.; Takui, T.; Okada, K. *Synth. Met.* **2001**, *121*(1−3), 1808−1809. (c) Hedayatullah, M.; Thevenet, F.; Denivelle, L. *Tetrahedron Lett.* **1977**, *18*, 1595−1596.

Scheme 1. Preparations of *N*-Aryl-*N*-pyridylaminoxyls and Their Co Complexes

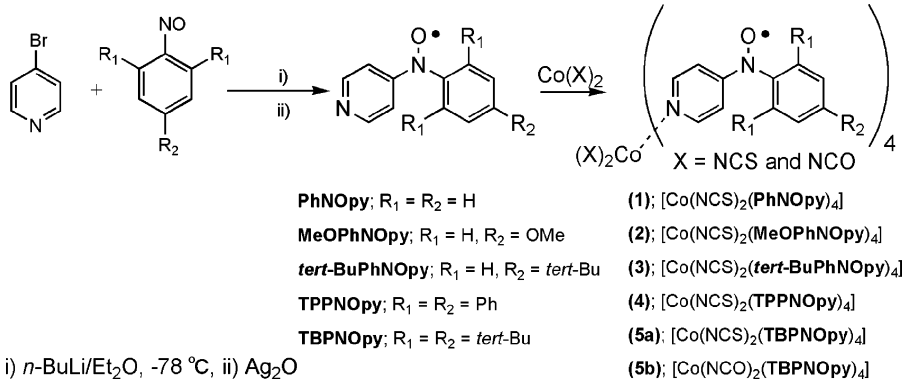

was prepared in a manner similar to **1** by using ***tert*-BuPhNOPy**. Complex **3** was obtained as dark-red chip crystals (114 mg): mp (dec) 157−159 °C, IR (KBr pellet) $\nu = 2067$ cm^{-1} (NCS); Anal. Calcd for $C_{62}H_{68}N_{10}O_4S_2Co$: C 65.30, H 6.01, N 12.28%; found: C 65.14, H 6.11, N 12.16%.

Tetrakis[4-{*N*-(2,4,6-Triphenylphenyl)-*N*-oxylamino}pyridine]di(thiocyanato-*N*)cobalt(II), [Co(NCS)$_2$(TPPNOPy)$_4$] (4). This was prepared in a manner similar to **1** by using **TPPNOPy**. Immediately after mixing, complex **4** was obtained as a dark-red powder (162 mg): mp (dec) 198−200 °C, IR (KBr pellet) $\nu = 2058$ cm^{-1} (NCS); Anal. Calcd for $C_{118}H_{84}N_{10}O_4S_2Co\cdot 5/2Et_2O$: C 75.98 H 5.13, N 7.20%; found: C 75.89, H 5.05, N 7.11%.

Tetrakis[4-{*N*-(2,4,6-Tri-*tert*-butylphenyl)-*N*-oxylamino}pyridine]di(thiocyanato-*N*)cobalt(II), [Co(NCS)$_2$(TBPNOPy)$_4$] (5a). This was prepared in a manner similar to **1** by using **TBPNOPy**. Complex **5a** was obtained as dark-red brick-like crystals (42 mg): mp (dec) 156−158 °C, IR (KBr pellet) $\nu = 2051$ cm^{-1} (NCS); Anal. Calcd for $C_{94}H_{132}N_{10}O_4S_2Co$: C 71.04, H 8.37, N 8.81%; found: C 71.19, H 8.52, N 8.54%.

Tetrakis[4-{*N*-(2,4,6-*tert*-Butylphenyl)-*N*-oxylamino}pyridine]di(isocyanato-*N*)cobalt(II), [Co(NCO)$_2$(TBPNOPy)$_4$] (5b). A solution of **TBPNOPy** (200 mg, 0.56 mmol) in diethyl ether (20 mL) and a solution of $Co(NO_3)_2\cdot 6H_2O$ (31 mg, 0.10 mmol) and KNCO (19 mg, 0.23 mmol) in methyl alcohol (3 mL) were mixed and then stirred for 10 min. The solvents were removed to dryness under reduced pressure. The dark-green solid obtained was dissolved in a small amount of dichloromethane (ca. 1 mL). Diethyl ether (10 mL) and *n*-hexane (15 mL) were added to the mixture and the volume of the solution was reduced to 15 mL on a rotary evaporator. The resulting precipitates were removed by filtration, and the filtrate was kept at −30 °C. The complex **5b** was obtained as dark-red brick-like crystals (115 mg): mp (dec) 88−90 °C; IR (KBr pellet) $\nu = 2198$ cm^{-1} (NCO); Anal. Calcd for $C_{94}H_{132}N_{10}O_6Co\cdot 2/3CH_2Cl_2$: C 70.46, H 8.33, N 8.68%; found: C 70.42, H 8.50, N 8.69%.

Results and Discussion

Molecular Design and Preparations. In this study, we attempted to modulate the intermolecular distance in the crystal lattice by varying the bulkiness and number of diamagnetic substituents. To this end, a *N*-aryl-*N*-pyridilaminoxyl was used as a frame for the ligand in the heterospin system. Taking the bulkiness of the substituent into account, a methoxy group and a *tert*-butyl group were selected and introduced at the 4-position of the phenyl ring. Furthermore, bulky substituents, a *tert*-butyl group and a phenyl ring, were introduced at the 2, 4, and 6-positions of the phenyl ring, in which the substituents at the 2 and 6-positions lie near the aminoxyl center. Those substituents were expected to play two important roles as follows. (1) The substituents prevent the access of neighboring molecules to the aminoxyl center. (2) They prevent the electron spin of aminoxyl from delocalizing onto the phenyl ring by sterically twisting the phenyl ring from the aminoxyl plane.

The intermolecular magnetic interactions in a crystalline state take place not only between the radical spin centers but also between the atoms bearing the spin density. To understand the magnetic coupling in a crystal lattice, therefore, it is necessary to know the spin distribution of the aminoxyl ligand. For the estimation of the spin density distributions in *N*-aryl-*N*-pyridylaminoxyls, **PhNOPy**, **MeOPhNOPy**, ***tert*-BuPhNOPy**, **TPPNOPy**, and **TBPNOPy**, a molecular orbital calculation based on the density function theory (DFT) was performed. The popular unrestricted B3LYP hybrid density functional[16,17] with the standard split valence 6-31G(d) basis set was used for the computation using the GAUSSIAN 98 program package. The molecular geometries of **PhNOPy**, **MeOPhNOPy**, and ***tert*-BuPhNOPy** were determined by MM2 calculation, and those of **TPPNOPy** and **TBPNOPy** were used from the data of X-ray analyses described in the following section. The spin density populations revealed by the calculation for five *N*-aryl-*N*-pyridylaminoxyls are shown in Figure S1 (Supporting Information). In monosubstituted aminoxyls, **PhNOPy**, **MeOPhNOPy**, and ***tert*-BuPhNOPy**, the spin density distributed onto both the benzene and pyridine rings, whereas in trisubstituted aminoxyls, **TPPNOPy** and **TBPNOPy**, it distributed mainly onto the pyridine ring. The insignificant spin distribution onto the phenyl ring is due to the large dihedral angle between the phenyl ring

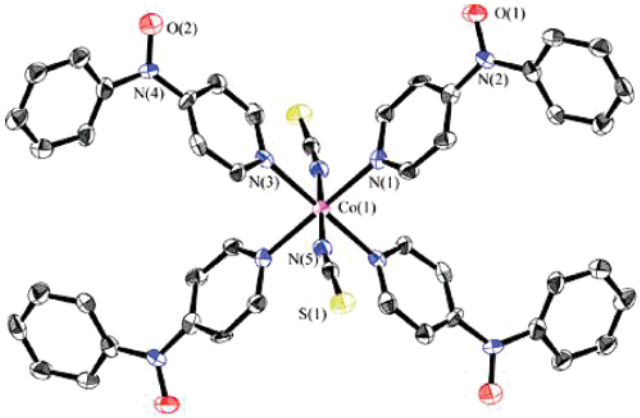

Figure 1. ORTEP drawing of the molecular structure of **1**. Hydrogen atoms are omitted for the sake of clarity.

(16) Becke, A. D. *Phys. Rev.* **1988**, *A38*, 3098.
(17) Lee, C.; Yang, W.; Parr, R. G. *Phys. Rev.* **1988**, *B37*, 785.

Table 3. Selected Bond Lengths (Å) and Dihedral Angles (deg) for **1**, **2**, and **3**

1		2		3	
		Bond lengths (Å)			
Co−N(1)	2.205	Co−N(1)	2.214	Co−N(1)	2.198
		Co−N(3)	2.199		
Co−N(3)	2.200	Co−N(5)	2.201	Co−N(3)	2.209
		Co−N(7)	2.190		
Co−N(5)	2.075	Co−N(9)	2.075	Co−N(5)	2.063
		Co−N(10)	2.076		
		Dihedral angles (deg) between pyridine ring and XY plane			
CoN(1)N(3)−N(1)C(2)C(4)	67.75	N(1)N(3)N(5)N(7)−N(1)C(2)C(4)	76.41	Co(1)N(1)N(3)−N(1)C(2)C(4)	71.46
CoN(1)N(3)−N(3)C(13)C(15)	69.53	N(1)N(3)N(5)N(7)−N(3)C(14)C(16)	61.85	Co(1)N(1)N(3)−N(3)C(17)C(19)	61.76
		N(1)N(3)N(5)N(7)−N(5)C(26)C(28)	71.12		
		N(1)N(3)N(5)N(7)−N(7)C(38)C(40)	63.82		
		Dihedral angles (deg) between pyridine ring and aminoxyl plane			
N(1)C(2)C(4)−O(1)N(2)C(3)	27.78	N(1)C(2)C(4)−O(1)N(2)C(3)	15.13	N(1)C(2)C(4)−O(1)N(2)C(3)	24.79
N(3)C(13)C(15)−O(2)N(4)C(14)	24.72	N(3)C(14)C(16)−O(3)N(4)C(15)	27.54	N(3)C(17)C(19)−O(2)N(4)C(18)	8.30
		N(5)C(26)C(28)−O(5)N(6)C(27)	9.00		
		N(7)C(38)C(40)−O(7)N(8)C(39)	28.13		
		Dihedral angles (deg) between phenyl ring and aminoxyl plane			
C(7) C(9) C(11)−O(1)N(2)C(6)	29.08	O(1)N(2)C(6)−C(7)C(9)C(11)	32.02	O(1)N(2)C(6)−C(7)C(9)C(11)	34.15
		O(3)N(4)C(18)−C(19)C(21)C(23)	26.52		
O(2)N(4)C(17)−C(18)C(20)C(22)	31.58	O(5)N(6)C(30)−C(31)C(33)C(35)	41.30	O(2)N(4)C(21)−C(22)C(24)C(26)	40.88
		O(7)N(8)C(42)−C(43)C(45)C(47)	25.74		

and the aminoxyl plane caused by the bulky substituents at the 2- and 6-positions of the phenyl ring, as expected.

As shown in Scheme 1, all the *N*-aryl-*N*-pyridylaminoxyls were prepared using similar procedures: metalation of 4-bromopyridine, a reaction with corresponding nitroso derivatives to give hydroxyamine derivatives, and oxidation with freshly prepared Ag_2O. All nitroso derivatives were prepared by procedures (or modified versions thereof) reported in the literature.[15] Although analogous **4NOpy** is unstable in a solid state, the *N*-aryl-*N*-pyridylaminoxyls were relatively stable in a solid state. Indeed, trisubstituted *N*-aryl-*N*-pyridylaminoxyls, **TPPNOpy** and **TBPNOpy**, were obtained as single crystals and their molecular structures were revealed by X-ray crystallography.

The 1:4 complexes of high-spin cobalt(II) with *N*-aryl-*N*-pyridylaminoxyls, $[Co(NCS)_2($**PhNOpy**$)_4]$ (**1**), $[Co(NCS)_2($**MeOPhNOpy**$)_4]$ (**2**), $[Co(NCS)_2($***tert*****-BuPhNOpy**$)_4]$ (**3**), $[Co(NCS)_2($**TBPNOpy**$)_4]$ (**5a**), and $[Co(NCO)_2($**TBPNOpy**$)_4]$ (**5b**), were prepared by mixing the solutions of $Co(NCS)_2$ (or a mixture of $Co(NO_3)_2$ and KNCO for **5b**) and the corresponding *N*-aryl-*N*-pyridylaminoxyls in 1:4 ratios at room temperature. The complexes were crystallized from suitable solvents at −30 °C and were obtained as dark-red crystals. Complex **4** was obtained only as a red microcrystal under similar conditions.

Crystal Structural Analysis. The single crystals of two *N*-aryl-*N*-pyridylaminoxyls, **TPPNOpy** and **TBPNOpy**, and five cobalt(II) complexes, **1**, **2**, **3**, **5a**, and **5b**, were analyzed by X-ray crystallography. A single crystal of **4** with a size amenable to the X-ray analysis could not be obtained.

The crystals contain one molecule for complex **2** and two molecules for complex **5a** and **5b** of diethyl ether per unit cell. Five cobalt(II) complexes have a similar hexacoordinated structure, in which each cobalt ion is surrounded by four nitrogen atoms of pyridine rings (N_{Py}) at the basal plane and two counterions at the apical positions.

(A) $[Co(NCS)_2(PhNOpy)_4]$ (1), $[Co(NCS)_2(MeOPhNOpy)_4]$ (2), and $[Co(NCS)_2($*tert*-BuPhNOpy**$)_4]$ (3).** In molecular geometry, the three complexes are compressed octahedrons with symmetry centered at the cobalt ion for **1** and **3** and with no symmetric center for **2**. The ORTEP drawing of the molecular structure of **1** is demonstrated in Figure 1. The drawings for **2** and **3** are shown in Figure S2 (Supporting Information).

In the octahedral structure of three complexes, the bond lengths ($Co-N_{NCS}$) between the axial ligand and the cobalt ion are short by 0.13−0.14 Å compared with those ($Co-N_{Py}$) between the nitrogen of pyridine and the cobalt ion. The bond lengths of $Co-N_{NCS}$ are 2.075, 2.075 and 2.076, and 2.063 Å for **1**, **2**, and **3**, respectively. The dihedral angles between the pyridine ring and the XY plane defined by the nitrogen atoms of four pyridines in three complexes are in the range of 62−76°, which may affect the zero-field splitting parameters of the complexes. The dihedral angles between the pyridine ring and the aminoxyl plane and between the phenyl ring and the aminoxyl plane are 9−28 and 26−41°, respectively. The former angles suggest that the magnetic coupling between the aminoxyl and the cobalt ion takes place effectively. Both dihedral angles are relatively small (the latter angles are slightly larger than the former), indicating that the aminoxyl spins delocalize not only on the pyridine ring but also on the phenyl ring, as expected by the calculation. In the crystalline state for three complexes, therefore, the magnetic interaction resulting from the intermolecular short contacts between the phenyl ring and the neighboring molecules must be taken into account. Observed bond lengths and dihedral angles are similar to those for $[Co(NCS)_2($**4NOpy**$)_4]$ reported previously.[10] The selected bond lengths and the dihedral angles for **1**−**3** are summarized in Table 3.

The three complexes have a similar crystal structure, shown in Figure 2 for **1** and Figure S2 (Supporting Information) for **2** and **3**, respectively. In the crystal lattice, there are two complex molecules tilting in the opposite direction of each other, which are shown by the green and tan colors in Figure 2. Each molecule aligns in one direction to form a chain structure (chain A and chain B in Figure 2a), and the resulting chains alternately align in parallel. One complex molecule (for example, the green molecule in Figure 2b) is surrounded by six complex molecules (two green and four tan colored molecules) at a significantly

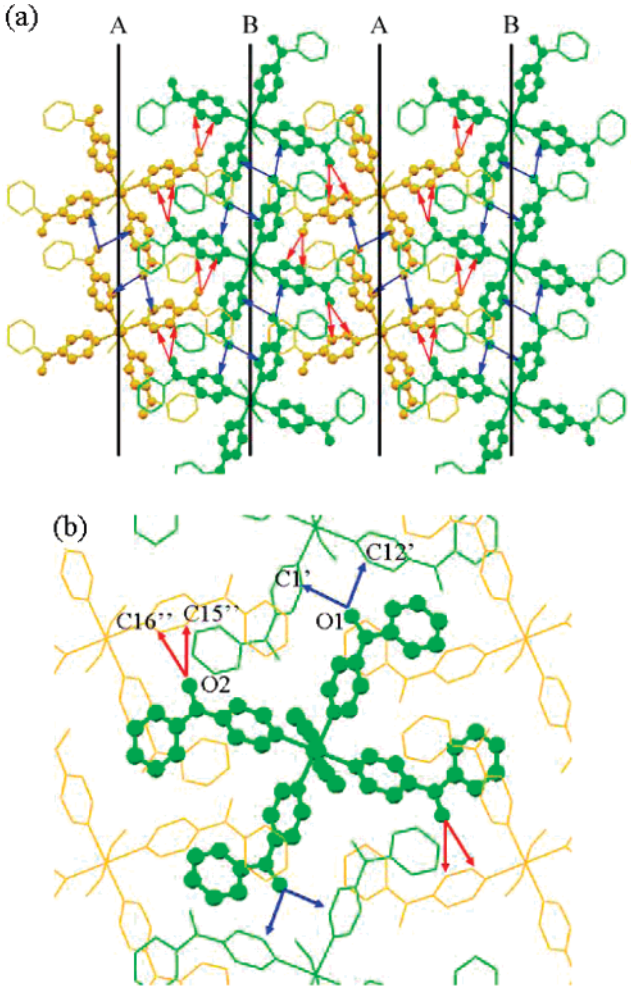

Figure 2. (a) Packing diagram along the *bc* plane showing 1D chains (chain A and B) and 2D plane and (b) short contacts with the surrounding molecules for **1**. The intermolecular short distances between the aminoxyl center and the α-, *β*-carbon of pyridine in the neighboring molecules are indicated by red and blue arrows, which show the inter- and intrachain short contacts, respectively.

Table 4. Intermolecular Distances between the Aminoxyl Center and the α-, *β*-Carbon of Pyridine Groups in the Neighboring Molecule in the Crystals of **1**, **2**, and **3**

1, Å		**2**, Å		**3**, Å	
O1···C1′	3.293	O1···C17′	3.181	O1···C4′	3.138
		O1···C25′	3.159		
O1···C12′	3.196	O3···C40″	3.110	O1···C5′	3.161
		O3···C41″	2.973		
O2···C15″	3.144	O5···C1‴	3.089	O2···C1″	2.981
		O5···C37‴	3.206		
O2···C16″	3.084	O7···C13⁗	3.135	O2···C2″	3.057
		O7···C14⁗	3.002		

short distance (<4.0 Å) resulting in intermolecular magnetic coupling. In addition to the distance between the aminoxyl centers ($r_{NO-NO'}$ = 3.99−4.38 Å), the four aminoxyl centers in a molecule locate in the distance range of 3.0−3.3 Å from the α-, *β*-carbons of pyridines in the surrounding six molecules (Figure 2b) to form a 2D spin network. The short contacts are indicated by red and blue arrows in Figure 2 and are listed in Table 4. The red and blue arrows also show the intra- and interchain short contacts, respectively. On the other hand, there are no short contacts between the cobalt ions, and the shortest distance for Co−Co′ is 8.92−10.77 Å. All cobalt ions in the plane reside in the resulting same one.

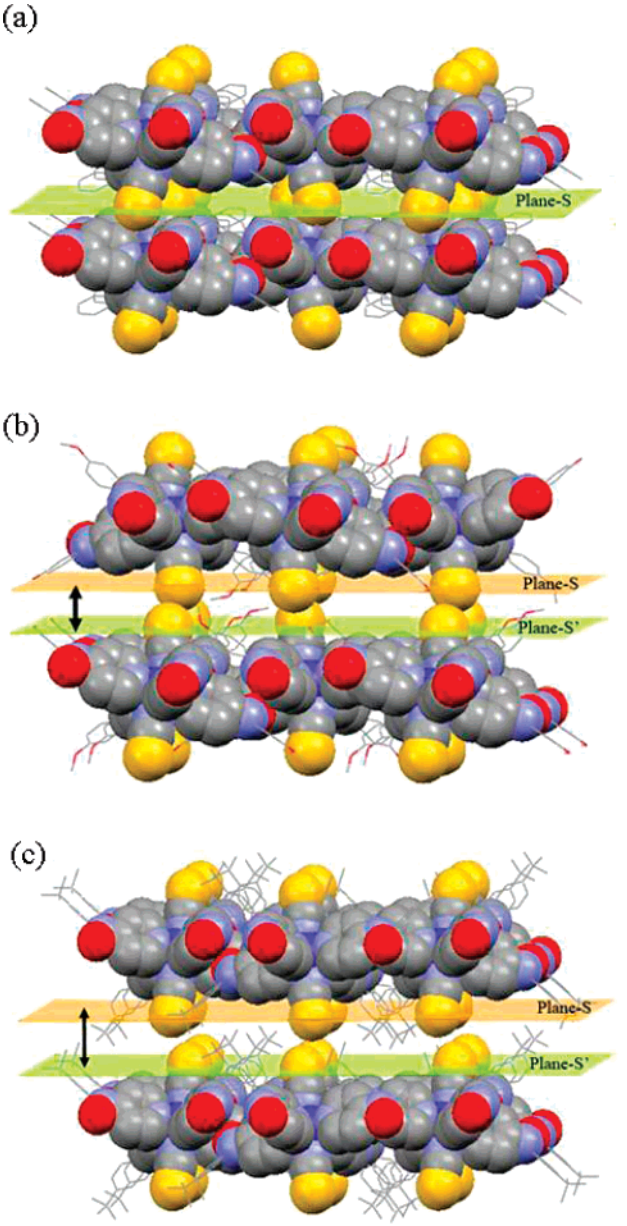

Figure 3. Packing diagrams of (a) **1**, (b) **2**, and (c) **3** showing two layers of the 2D-plane units. Plane-S and plane-S′ are those containing the sulfur atoms of the axial ligands.

The resulting planes are layered parallel to the *bc* plane for **1** and **3** and the *ab* plane for **2** to form the 3D structure. As observed in Figure 3, the substituents at the 4-position of the phenyl ring in these three complexes project the space between the two planes. Therefore, the distances between the planes depend on the bulkiness of the substituents. When the distances between the 2D planes were compared by using the plane (plane-S and -S′ in Figure 3) containing the sulfur atoms of the axial ligands, the distance between plane-S and plane-S′ is ∼0, 2.66, and 4.11 Å for **1**, **2**, and **3**, respectively. In addition, the distance between the cobalt planes, which is defined by all cobalt ions in the plane, is 8.91, 11.52, and 13.10 Å for **1**, **2**, and **3**, respectively. Observed distances are consistent with the order of the bulkiness of the substituents (−H < −OMe <−*tert*-Bu),

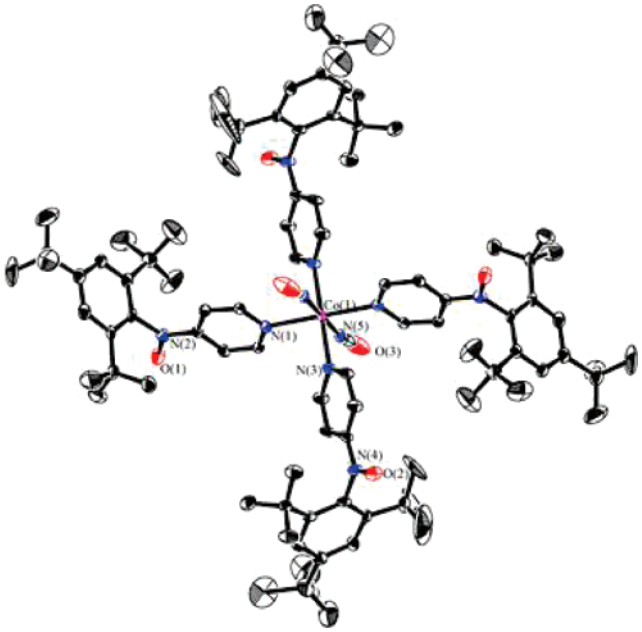

Figure 4. ORTEP drawing of the molecular structure of **5b**. Hydrogen atoms are omitted for the sake of clarity.

indicating that the substituent at the 4-position of the phenyl ring controls the distance between the 2D planes in the crystal.

The existence of the two complex molecules with different tilting directions in the 2D planes and the distance between the 2D planes strongly affected the magnetic properties of the complexes, as discussed in the section on the magnetic properties for the complexes. A 3D structure similar to **1** was also observed in an analogous complex, $[Co(NCS)_2(\mathbf{4NOpy})_4]$.[10]

(B) TPPNOpy, TBPNOpy, $[Co(NCS)_2(TBPNOpy)_4]$ (5a) and $[Co(NCO)_2(TBPNOpy)_4]$ (5b). (B)-1 TPPNOpy and TBPNOpy. The bond angle of C(3)N(2)C(6) in aminoxyl units is 123.4° for **TPPNOpy** and 124.2° for **TBPNOpy**, both close to that for **PhNOpy** (125.1°). On the other hand, the dihedral angles between the phenyl and pyridine rings are largely twisted by the 2,6-substituents compared with the angle (51.09°) for **PhNOpy**, being 76.63 and 88.51° for **TPPNOpy** and **TBPNOpy**, respectively. The dihedral angles between the phenyl ring and the aminoxyl plane and between the pyridine ring and the aminoxyl plane for **TBPNOpy** are 87 and 3.6°, respectively, indicating that the aminoxyl spin mainly delocalized on the pyridine ring. Similarly, **TPPNOpy** has dihedral angles of 71 and 68° for the former and 8.4 and 3.3° for the latter. The ORTEP drawings of the molecular structure of **TPPNOpy** and **TBPNOpy** are shown in Figure S3 (Supporting Information).

(B)-2 $[Co(NCS)_2(TBPNOpy)_4]$ (5a) and $[Co(NCO)_2(TBPNOpy)_4]$ (5b). The molecular geometry for both **5a** and **5b** is also a compressed octahedron with symmetry centered at the cobalt ion. The ORTEP drawing of the molecular structure of **5b** is shown in Figure 4.

The bond lengths ($Co-N_{NCX}$) between the axial ligand and the cobalt ion are short by 0.10−0.18 Å compared with those ($Co-N_{Py}$) between the nitrogen of pyridine and the cobalt ion. Both dihedral angles between the aminoxyl plane and the pyridine ring and between the aminoxyl radicals and the XY plane containing cobalt(II) ion become small compared with those for monosubstituted complexes. The former and latter dihedral angles are in the range of 2.3−6.9° and 58−62°, respectively. On the other hand, the dihedral angles between the aminoxyl plane and the phenyl ring become large (80−86°), as expected. No large differences in the molecular structure of **TBPNOpy** between the bound and free pyridine ligands were observed. The large dihedral angles arising from the bulky substituents at the 2 and 6-position of the phenyl ring mean that the distributions of the electron spin on the phenyl ring become insignificant. The selected bond lengths and the dihedral angles for **5a** and **5b** together with **TBPNOpy** are summarized in Table 5. The complexes have a similar crystal structure in which short distances, within 4 Å, are observed neither between the aminoxyl radical centers nor between the radical center and the α and β carbons of the pyridine ring of the neighboring molecules. The distance between the cobalt ions is in the range of 10.2−20.3 Å. Therefore, **5a** and **5b** having 2,4,6,-trisubstituted benzene units are expected to suppress effectively the intermolecular interaction in the crystal state. The crystal packings for **5a** and **5b** are shown in Figure S4 (Supporting Information) and Figure 5, respectively.

In these five complexes, the substituents on the phenyl ring effectively tune the intermolecular distance in the crystal lattices. The substituent at the 4-position of the phenyl ring in monosubstituted complexes modulates the distance between the planes, and the distance increases according to the bulkiness of the substituent. The distance between the planes is large in the order of **1**, **2**, and **3**. On the other hand, the bulky substituents at the 2, 4, and 6-positions of the phenyl ring in the complex control the intermolecular distance. In the crystal structures of **5a** and **5b** having *tert*-butyl groups at the 2, 4, and 6-positions of the phenyl ring, significant short contacts within 4 Å among the molecules were not observed, indicating that the complex molecules are magnetically well separated.

Magnetic Properties. The magnetic properties of the 1:4 complexes **1**, **2**, **3**, **4**, **5a**, and **5b** were investigated using SQUID magneto/susceptometry.

(A) $[Co(NCS)_2(PhNOpy)_4]$ (1), $[Co(NCS)_2(MeOPhNOpy)_4]$ (2), and $[Co(NCS)_2(tert\text{-}BuPhNOpy)_4]$ (3). The dc magnetic susceptibilities (χ_{mol}) for the pulverized samples of three complexes were measured at a constant field of 5 kOe in the temperature range of 2−300 K. Temperature dependence of the χ_{mol} of **1**, **2**, and **3** is shown as χ_{mol} vs T and χ_{mol}^{-1} vs T plots in the entire temperature region in Figure 6a−c, respectively, and as a $\chi_{mol}T$ vs T plot in the range of 2−50 K in Figure 6d.

The χ_{mol}^{-1} vs T plots of three complexes were analyzed by the Curie−Weiss equation, $\chi_{mol} = C/(T - \theta)$ where C and θ are Curie and Weiss constants, respectively. Best fits of the χ_{mol} data above 100 K for **1**, **2**, and **3**, to the Curie−Weiss equation gave C = 4.78, 4.92, and 5.23 $cm^3mol^{-1}K$ and θ = −6.74, −32.4, and −41.7 K, respectively. These Curie constants are much higher than the spin-only value of 3.38 $cm^3mol^{-1}K$ expected for an isolated one high-spin Co(II) ion ($S = {}^3/_2$, $g_{Co} = 2.00$) and four aminoxyls ($S = {}^1/_2$ and $g_{NO} = 2.00$) owing to the orbital contribution of the Co(II) ion.[18] The negative Weiss constants suggest the presence of antiferromagnetic coupling.

In the χ_{mol} vs T plot of **1** (Figure 6a), a sharp maximum at 22 K was observed, indicating that the antiferromagnetic

(18) Hossain, M. J.; Yamasaki, M.; Mikuriya, M.; Kuribayashi, A.; Sakiyama, H. *Inorg. Chem.* **2002**, *41*, 4058−4062.

Table 5. Selected Bond Lengths (Å) and Dihedral Angles (deg) for **5a**, **5b**, and **TBPNOpy**

5a		5b		TBPNOpy	
		Bond lengths (Å)			
Co−N(1)	2.191	Co−N(1)	2.202		
Co−N(3)	2.219	Co−N(3)	2.240		
Co−N(5)	2.090	Co−N(5)	2.060		
		Dihedral angles (deg) between pyridine ring and XY plane			
CoN(1)N(3)−N(1)C(2)C(4)	57.87	CoN(1)N(3)−N(1)C(2)C(4)	59.58		
CoN(1)N(3)−N(3)C(25)C(27)	60.19	CoN(1)N(3)−N(3)C(25)C(27)	58.15		
		Dihedral angles (deg) between pyridine ring and aminoxyl plane			
N(1)C(2)C(4)−O(1)N(2)C(3)	2.33	N(1)C(2)C(4)−O(1)N(2)C(3)	2.53	N(1)C(2)C(4)−O(1)N(2)C(3)	3.57
N(3)C(25)C(27)−O(2)N(4)C(26)	5.80	N(3)C(25)C(27)−O(2)N(4)C(26)	6.90		
		Dihedral angles (deg) between phenyl ring and aminoxyl plane			
O(1)N(2)C(6)−C(7)C(9)C(11)	84.26	O(1)N(2)C(6)−C(7)C(9)C(11)	85.72	O(1)N(2)C(6)−C(7)C(9)C(11)	86.84
O(2)N(4)C(29)−C(30)C(32)C(34)	79.73	O(2)N(4)C(29)−C(30)C(32)C(34)	79.95		

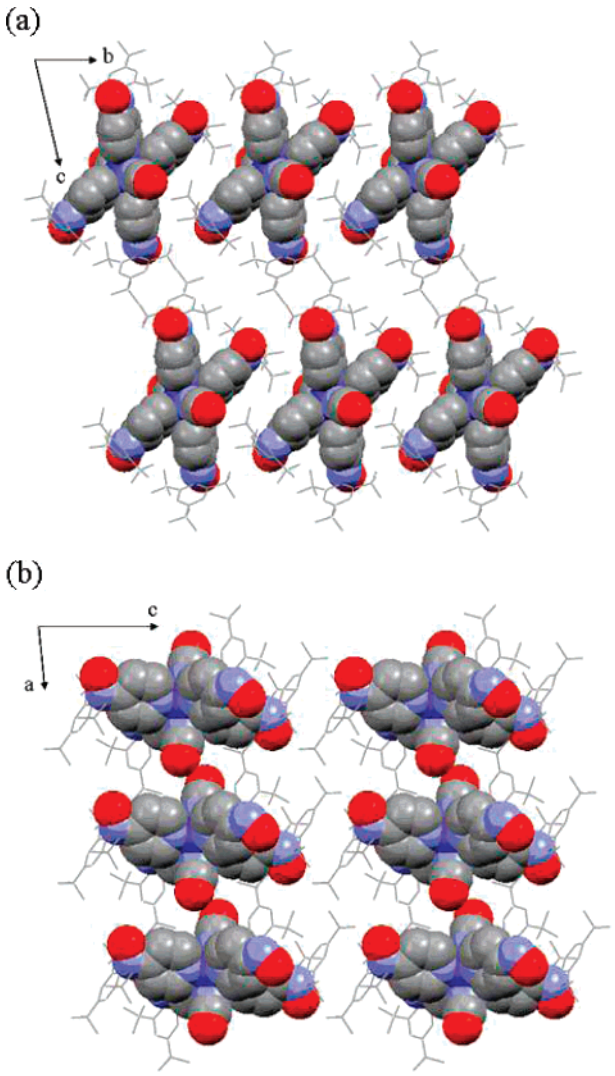

Figure 5. Crystal packings with the space filling model (C, gray; O, red; and N, blue) projecting along the (a) *a*-axis and (b) *b*-axis for **5b**. Aryl units of **TBPNOpy** in **5b** are indicated by the gray lines.

ordering operated below the temperature.[19] From the temperature of the sharp maximum of χ_{mol}, the Neel temperature, T_N, was defined to be 22 K for **1**. The observed magnetic behavior was similar to that for $[Co(NCS)_2(\mathbf{4NOpy})_4]$, which has a T_N of 15 K.

In the $\chi_{mol}T$ vs T plot of **2** at a constant field of 5 kOe (Figure 6d), the $\chi_{mol}T$ values gradually decreased on cooling until 10 K, increased steeply to reach a maximum (1.28 $cm^3mol^{-1}K$) at ca. 3 K, and then decreased. The observed thermal profile of χ_{mol} values below 10 K strongly depended on the applying field. The χ_{mol} vs T plots at constant fields of 1.0, 0.5, and 0.1 kOe are shown in Figure 7a. The maximum χ_{mol} value (1.08 cm^3mol^{-1}) at 2.3 K appeared at 1.0 kOe and the peak-top temperature slightly shifted to a higher temperature with a decrease in the external field. This field dependence of χ_{mol} suggests an antiferromagnetic transition.[20] To determine the Neel temperature, T_N, ac magnetic susceptibility measurements were carried out with an ac field of 3.9 Oe at 997, 99.9, and 1 Hz. In the temperature dependence of ac molar magnetic susceptibilities, in-phase signals (χ'_{mol}) without frequency dependence were observed and showed the maximum at 2.9 K, whereas out-of phase signals (χ''_{mol}) were extremely weak (Figure 7b). From the observed peak-top temperature of the χ'_{mol} signal, the T_N value of **2** was determined to be 2.9 K.

In the χ_{mol} vs T plot of **3** (Figure 6d), the thermal profile of χ_{mol} values below 10 K was similar to that for **2** and also showed the dependence of applying the external field. At a constant field less than 1 kOe, the $\chi_{mol}T$ values steeply increased below 5 K, indicating that a long-range magnetic ordering of magnetic spin takes place. To characterize a long-range magnetic ordering, dc magnetic measurements using a sequence of zero field-cooled magnetization (ZFCM), field-cooled magnetization (FCM), and remnant magnetization (RM) and the ac magnetic measurements in a zero dc field with a 3.9 Oe ac field at 997, 99.9, and 1 Hz were carried out in the temperature range of 10−1.9 K. The dc and ac magnetic measurements are shown in Figure 8a and b, respectively.

The molar magnetization, M_{mol}, in the FCM measurement at a constant field of 4.7 Oe increased rapidly below ca. 5 K, reached a value of 977 $cm^3\ mol^{-1}Oe$ at 3.5 K, and then slightly increased below it. The derivative curve, dM/dT, of the FCM measurement gave an extremum at 4.5 K corresponding to the critical temperature, T_c. On the other hand, the M_{mol} values in the ZFCM measurement showed a relatively sharp maximum at ca. 4.5 K and a large discrepancy in M_{mol} values between the ZFCM and FCM measurements was observed below T_c = 4.5 K (Figure 8a). In the RM measurement, the M_{mol} value,

(19) (a) King, P.; Clérac, R.; Anson, C. E.; Coulon, C.; Powell, A. *Inorg. Chem.* **2003**, *42*, 3492−3500. (b) Aoki, C.; Ishida, T.; Nogami, T. *Inorg. Chem.* **2003**, *42*, 7616−7625.

(20) Manson, J. L.; Huang, Q.; Lynn, J. W.; Koo, H. J.; Whangbo, M. H.; Bateman, R.; Otsuka, T.; Wada, N.; Argyriou, D. N.; Miller, J. S. *J. Am. Chem. Soc.* **2001**, *123*, 162−172.

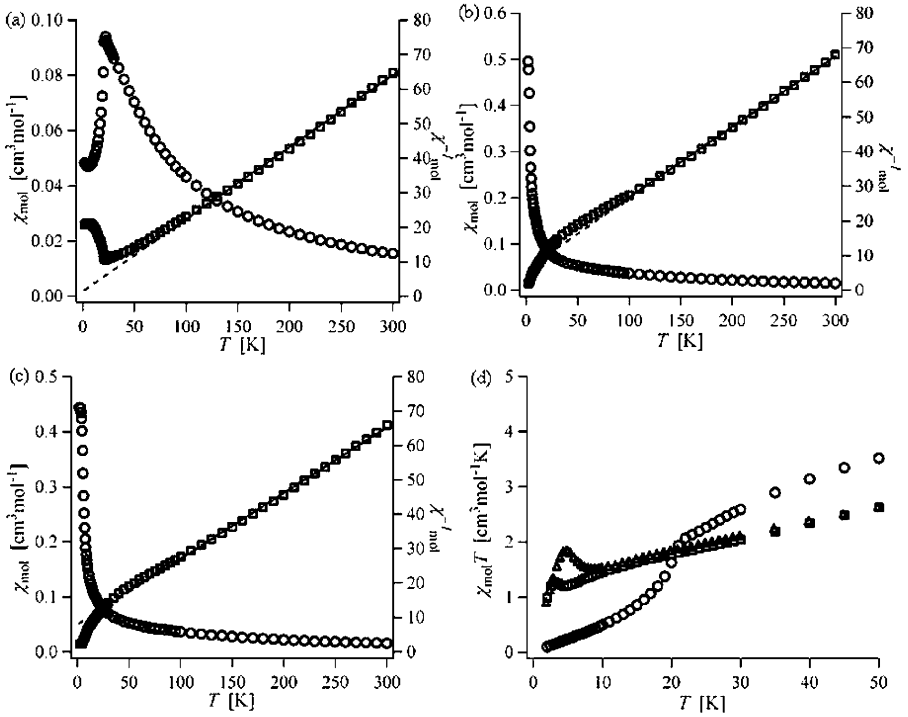

Figure 6. Plots of χ_{mol} vs T (○) and $\chi_{mol}{}^{-1}$ vs T (□) for the pulverized samples of (a) **1**, (b) **2**, and (c) **3** and (d) the plots of $\chi_{mol}T$ vs T in the temperature range 1.9−50 K for **1**(○), **2**(□), and **3**(△). The dashed lines are the fitting results from a Curie−Weiss equation; see the text for the fitting parameters.

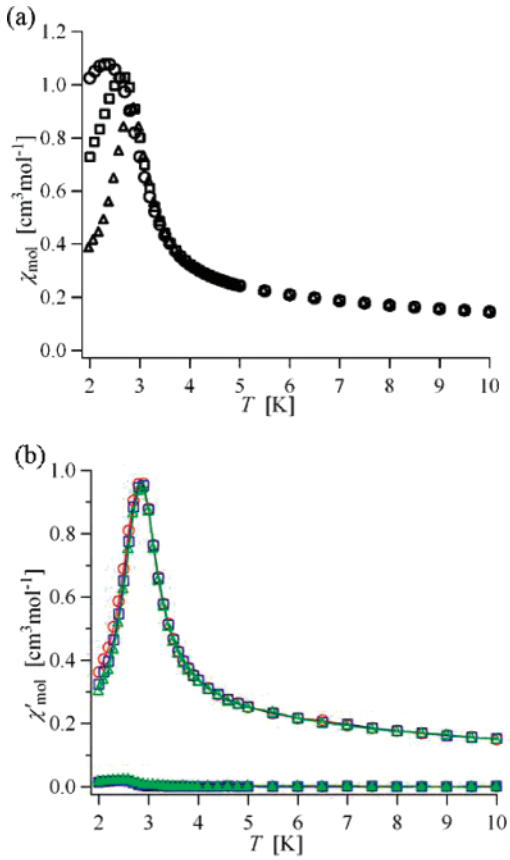

Figure 7. Plots of (a) χ_{mol} vs T at a constant field of 1(○), 0.5(□), and 0.1(△) kOe and (b) χ'_{mol} and χ''_{mol} vs T at an ac field of 3.9 Oe at 997 (△), 99.9 (□), and 1 (○) Hz for the pulverized sample of **2**.

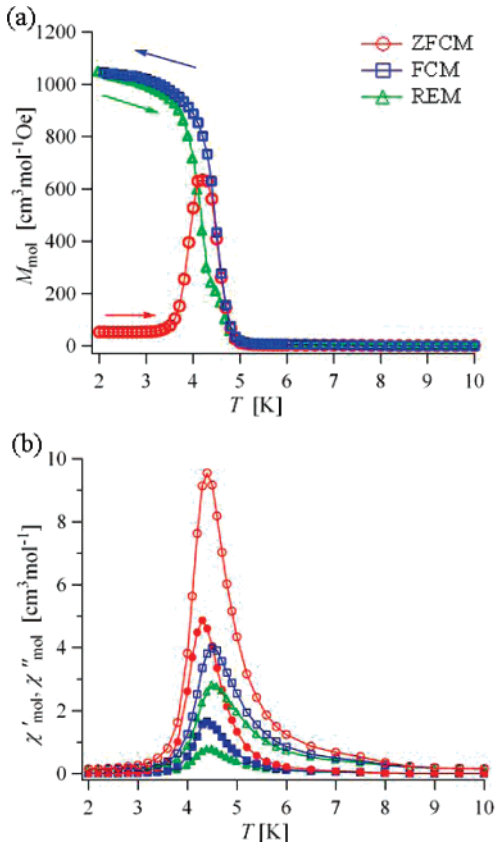

Figure 8. (a) M vs T plot in ZFCM (○), FCM (□), and RM (△) measurements and (b) χ'_{mol} (open) and χ''_{mol} (filled) vs T plots at 997 (△), 99.9 (□), and 1 Hz (○) for the pulverized sample of **3**. Solid lines are visual guides.

which was 1046 cm^{3}mol^{-1}Oe at 2.0 K, decreased nearly along the curve for the FCM measurement upon warming and then disappeared above 5 K. In ac magnetic susceptibility measurements, both χ'_{mol} and χ''_{mol} signals with frequency dependence were observed (Figure 8b). In the χ'_{mol} and χ''_{mol} vs T plots, the thermal profiles of the χ'_{mol} and χ''_{mol} signals at each

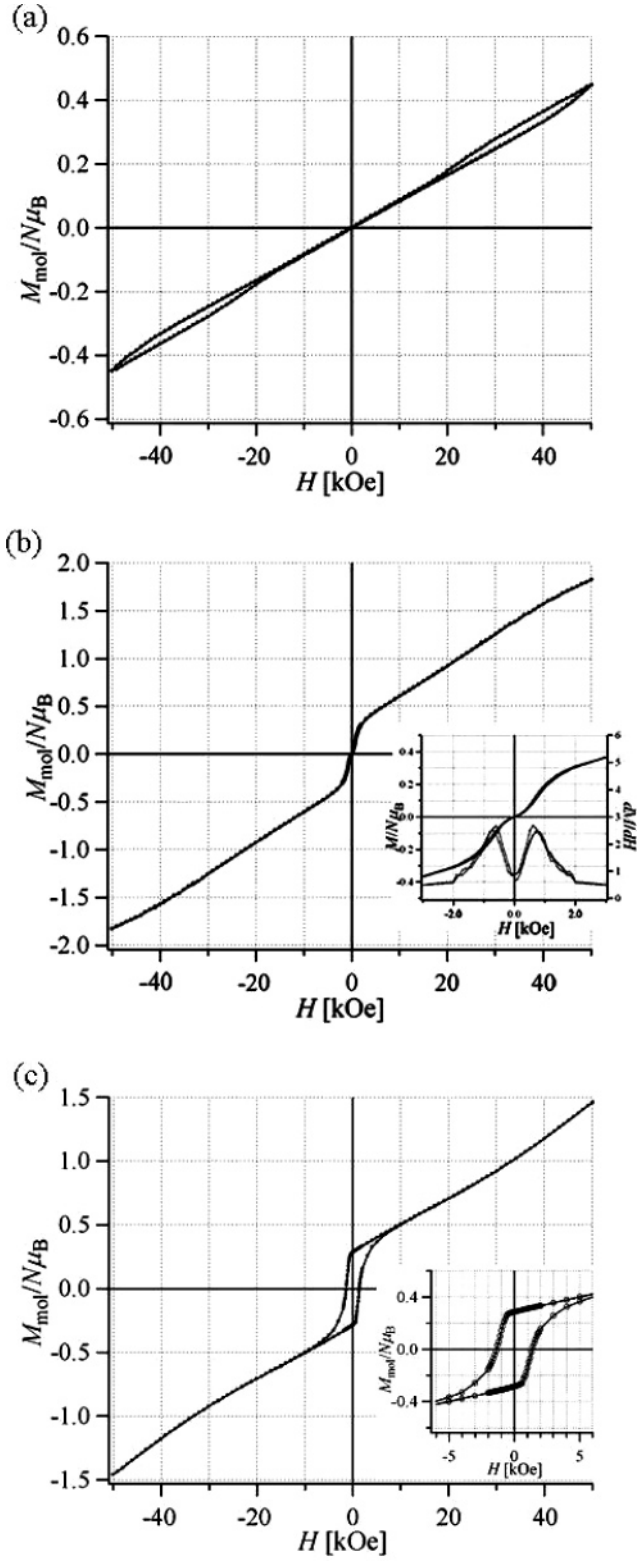

Figure 9. Figure 9. Plots of $M_{mol}/N\mu_B$ vs H for the pulverized samples of (a) **1**, (b) **2**, and (c) **3** at 1.9 K. The insets in (b) and (c) show the detail in a low field (0−3 kOe) together with the dM/dH vs H plot and the field range of ±6 kOe, respectively.

frequency were similar to each other: the χ'_{mol} and χ''_{mol} signals decreased as the frequency increased and had peak-top temperatures of 4.7 and 4.3 K, respectively. The peak-top temperature of 4.7 K for the χ'_{mol} signals was consistent with the T_c obtained in the dc magnetic susceptibility measurements. The temperature of 4.7 K obtained for the χ'_{mol} signal was defined as the T_N for **3**.[21]

To investigate the antiferromagnetic nature of **1**, **2**, and **3** in more detail, M_{mol} was measured at 1.9 K, where the temperature is below T_N, in the field range −50 to +50 kOe. When the dc field varied in the range of −50 to +50 kOe, three complexes showed characteristic magnetic behavior. The $M_{mol}/N\mu_B$ vs H plots for **1**, **2**, and **3** at 1.9 K are shown in Figure 9.

The values of $M_{mol}/N\mu_B$ at 50 kOe are 0.45, 1.82, and 1.46 for **1**, **2**, and **3**, respectively, and do not reach the saturation magnetization, M_s, even at 50 kOe. They are 2.7−11 times smaller than the value of M_s ($5/N\mu_B$) calculated by $S_{total} = {}^5/_2$ (one Co(II) ion with the effective spin quantum number $S' = {}^1/_2$ and four aminoxyls with $S = {}^1/_2$ are coupled ferromagnetically) and $g = 2.00$, indicating that strong antiferromagnetic interaction takes place in the spin networks. The three complexes showed the characteristic magnetic profiles individually in the field dependence of magnetization. In the $M_{mol}/N\mu_B$ vs H plot of **1**, the $M_{mol}/N\mu_B$ values increased gradually and slightly, as the dc field increased from 0 to 50 kOe. As seen in Figure 8a, a small discrepancy in the M_{mol} value on increasing and reducing the field was observed. In a similar plot for **2**, the $M_{mol}/N\mu_B$ increased slightly until 0.3 kOe, increased steeply to 0.18 at 1 kOe, and then increased linearly. This field dependence of $M_{mol}/N\mu_B$ values in a low field range might indicate the phase transition from an antiferromagnet phase to a spin-flop phase.[22] From the dM/dH vs H plot (inset in Figure 9b), an anomalous point corresponding to the spin-flop field at 1.9 K, H_{sp}, was determined to be 0.7 kOe. On the other hand, the $M_{mol}/N\mu_B$ values for **3** steeply increased to 0.3 $N\mu_B$ in 0−1.0 kOe and then increased with the curvature having a convex downward at above 1 kOe. The curvature suggests a possible spin-flop transition on applying a further field. Furthermore, interestingly, the complex **3** showed a hysteresis with respect to the field. The hysteresis loop with a remnant magnetization, M_r, of 0.29 $N\mu_B$ and a coercive force, H_c, of 1.3 kOe at 1.9 K is shown in Figure 9c. This magnetic behavior is typical of a canted antiferromagnet (a weak ferromagnet).[21]

The antiferromagnetic behavior of the three complexes was closely related with their crystal structure revealed by X-ray crystallography. The proximity of N(O)−C_β (or C_α) between the molecules, which were often observed in analogous heterospin complexes, leads to the antiferromagnetic (or ferromagnetic) coupling. In these complexes, the antiferromagnetic couplings operate predominantly to form the antiferromagnetic 2D planes. The difference in the magnetic behavior among the three complexes was caused by antiferromagnetic interaction between the 2D planes. The results of dc magnetic susceptibility measurements suggested that the antiferromagnetic interaction between the 2D planes decreases in the order of **1**, **2**, and **3** and becomes insignificant in **3**. The observed order of the magnitude of antiferromagnetic coupling in the three complexes is consistent with that for the distance between the 2D planes, **1** < **2** < **3**, (Figure 3). Notably, only **3** having a similar local structure in the 2D plane exhibits the magnetic behavior of a canted antiferromagnet, indicating that the magnetic interaction between the 2D planes counteracts the magnetic behavior for a canted

(21) Kim, J.; Han, S. J.; Pokhodnya, K. I.; Migliori, J. M.; Miller, J. S. *Inorg. Chem.* **2005**, *44*, 6983−6988.
(22) Wang, X. Y.; Wang, L.; Wang, Z. M.; Su, G.; Gao, S. *Chem. Mater.* **2005**, *17*, 6369−6380.

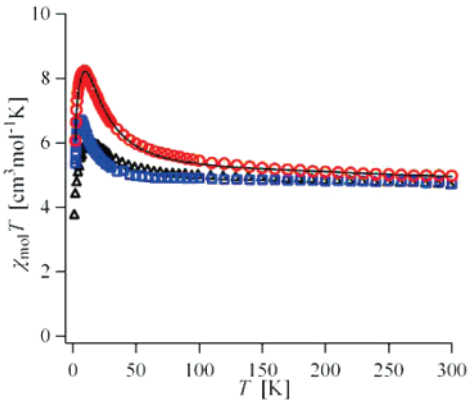

Figure 10. Plot of $\chi_{mol}T$ vs T for the pulverized samples of **4** (△), **5a** (□), and **5b** (○). The solid line for **5b** is the fitting result from the ligand field theory model; see the text for the fitting parameters.

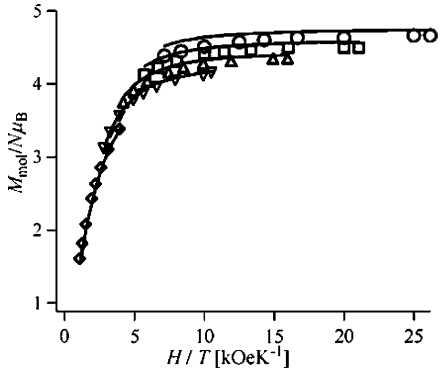

Figure 11. Plot of $M_{mol}/N\mu_B$ vs H/T at 0.8(◇), 20(▽), 30(△), 40(□), and 50(○) kOe for the pulverized sample of **5b**. The solid lines are the fitting results from the ligand field theory model; see the text for the fitting parameters.

antiferromagnet in the 2D plane. Similar magnetic behavior based on local and structural anisotropies in a low dimension was reported previously.[23]

(B) [Co(NCS)$_2$(TPPNOpy)$_4$] (4), [Co(NCS)$_2$(TBPNOpy)$_4$] (5a), and [Co(NCO)$_2$(TBPNOpy)$_4$] (5b). (B-1) Dc Magnetic Susceptibility Measurements in Microcrystalline State. The dc magnetic susceptibility of pulverized samples of the three complexes was measured at a constant field of 5 kOe in the temperature range of 2−300 K. The thermal profiles of χ_{mol} for the three complexes are similar, which are shown as χ_{mol} vs T and χ_{mol}^{-1} vs T plots in Figure S5 (Supporting Information) and a $\chi_{mol}T$ vs T plot in Figure 10. The χ_{mol} data above 100 K in the χ_{mol}^{-1} vs T plots for **4**, **5a**, and **5b** were analyzed by the Curie−Weiss equation (Figure S5a−c, Supporting Information) and gave $C = 4.57$, 4.75, and 4.75 cm^{3}mol^{-1}K and $\theta = 10.1$, 2.04, and 13.4 K, respectively. These Curie constants are similar to those (4.78−5.23 cm^{3}mol^{-1}K) for the monosubstituted complexes. The positive Weiss constants clearly indicate the presence of ferromagnetic couplings. In the $\chi_{mol}T$ vs T plots for the three complexes, the $\chi_{mol}T$ values were nearly constant until ca. 100 K, gradually increased on cooling, reached maxima at 15−5.5 K, and then decreased. The maximum values of $\chi_{mol}T$ are 6.00, 6.71, and 8.22 cm^{3}mol^{-1}K for **4**, **5a**, and **5b**, respectively. They are larger than the value of 3.6 cm^{3}mol^{-1}K (4×0.375 for aminoxyls + 2.1 for [Co(NCS)$_2$(py)$_4$] with $S' = {}^1/_2$[24]) for the isolated four aminoxyl radicals and a cobalt(II) ion, which also indicate that ferromagnetic interaction takes place between the cobalt ion and the aminoxyls through pyridine ligand and the high-spin complexes with $S_{total} = {}^5/_2$ are produced below the temperature showing the maximum $\chi_{mol}T$ value. Observed thermal profiles in the low-temperature region (100−20 K) showed a clear contrast to those for **1**, **2**, and **3**, where the $\chi_{mol}T$ values for **4**, **5a**, and **5b** gradually increase on cooling, while those for **1**, **2**, and **3**, gradually decrease under similar conditions (Figure 6d). The increase in $\chi_{mol}T$ on cooling indicates that the intermolecular antiferromagnetic interactions observed in **1**, **2**, and **3** were effectively eliminated and the complex molecules would be magnetically isolated.

The dc field dependence of M_{mol} for the pulverized samples of **4**, **5a**, and **5b** was measured at 1.9, 2.0, 2.5, 3.0, 3.5, 4.0, 5.0, 6.0, and 7.0 K in the range of 0.8−50 kOe. In the plots of $M/N\mu_B$ vs H/T for the three complexes, typically large deviations from the Brillouin function[14,25] were observed, indicating that the zero-field splitting parameter D/k_B operated at the ground state. The plot of $M/N\mu_B$ vs H/T for **5b** is shown in Figure 11.

The field dependence of M_{mol} for the orientated sample of **5b** was measured at 0.43 K in the field range of ±50 kOe. In the $M_{mol}/N\mu_B$ vs H plot, the M_{mol} values gradually increased and reached a saturation magnetization, M_s, of 6.35 over 3 kOe as the field increased. The M_s value of 6.35 corresponds to that calculated with $S_{total} = {}^5/_2$ and $g = 2.54$. In the cycle of applying and reducing the field, a small discrepancy in M_{mol} values between the increase and the decrease in the field in the range of 0.5−2 and −(0.5−2) kOe was observed (Figure S6, Supporting Information).

(B-2) Ac Magnetic Susceptibility Measurements. Ac magnetic susceptibility measurements for the pulverized samples of **4**, **5a**, and **5b** were carried out. The measurements were made in a zero dc field with a 3.9 Oe ac field at 997−1 Hz and in the temperature range of 1.9−10 K. In all three complexes, χ'_{mol} and χ''_{mol} signals with frequency dependence were observed, indicating that the complexes had a slow magnetic relaxation for the reversal of the magnetism. The plots of $\chi'_{mol}T$ vs T and χ''_{mol} vs T for **4**, **5a**, and **5b** are shown in Figure 12a−c, respectively.

In the $\chi'_{mol}T$ vs T plot of **4**, the $\chi'_{mol}T$ values gradually decreased on cooling from 10 to 3.5 K and then steeply decreased with frequency dependence below 3.5 K, whereas in the same plots of **5a** and **5b**, they slightly increased and were nearly constant, respectively, until the temperature that the χ''_{mol} signals appeared. Although for **4** there are no data from X-ray crystallography, the decrease in the $\chi'_{mol}T$ values in the range of 10−3.5 K might indicate that the weak antiferromagnetic interaction operates intermolecularly. In the χ''_{mol} vs T plots for three complexes, the maxima of χ''_{mol} signals shifted to the lower temperature side as the frequency decreased. Complexes

(23) (a) Salah, M. B.; Vilminot, S.; Andre, G.; Richard-Plouet, M.; Mhiri, T.; Takagi, S.; Kurmoo, M. *J. Am. Chem. Soc.* **2006**, *128*, 7972−7981. (b) Takagami, N.; Ishida, T.; Nogami, T. *Bull. Chem. Soc. Jpn.* **2004**, *77*, 1125−1135. (c) Coronado, E.; Galan-Mascaros, J. R.; Gomez-Garcia, C. J.; Murcia-Martinez, A. *Chem.−Eur. J.* **2006**, *12*, 3484−3492. (d) Bellouard, F.; Clemente-Leon, M.; Coronado, E.; Galan-Mascaros, J. R.; Gomez-Garcia, C. J.; Romero, F.; Dunbar, K. R. *Eur. J. Inorg. Chem.* **2002**, *43*, 1603−1606.

(24) (a) Jankovics, H.; Daskalakis, M.; Raptopoulou, C. P.; Terzis, A.; Tangoulis, V.; Giapintzakis, J.; Kiss, T.; Salifouglou, A. *Inorg. Chem.* **2002**, *41*, 3366−3374. (b) Thuery, P.; Zarembowitch, J. *Inorg. Chem.* **1986**, *25*, 2001−2008. (c) Zarembowitch, J.; Kahn, O. *Inorg. Chem.* **1984**, *23*, 589−593.

(25) $M = NgS\mu_B B(x)$ where $B(x)$ is a Brillouin function, where $x = gS\mu_B H/k_B T$, and the other symbols have their usual meanings.

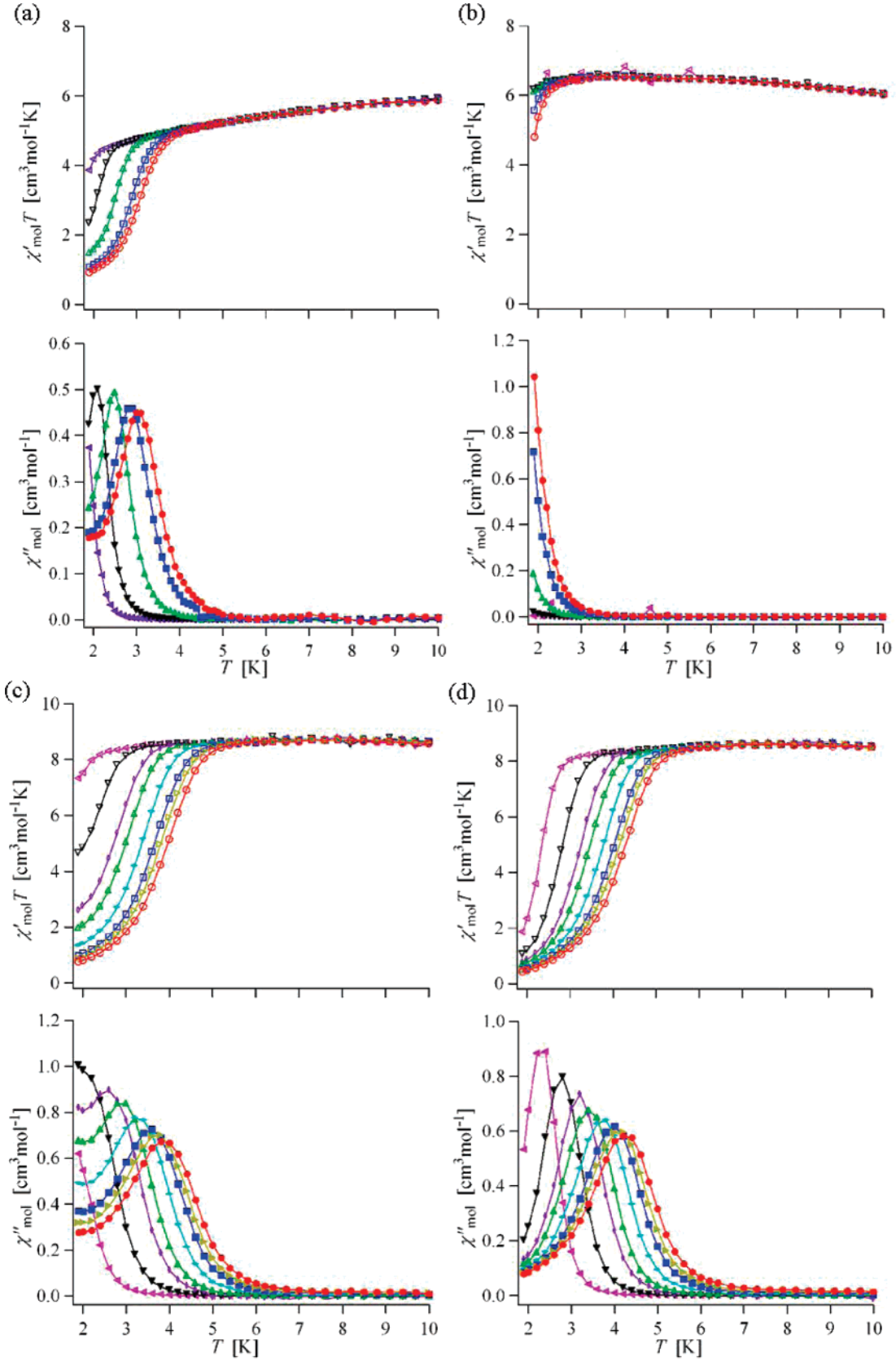

Figure 12. Plots of $\chi'_{mol}T$ vs T (upper) and χ''_{mol} vs T (lower) for the pulverized samples of (a) **4**, (b) **5a**, and (c) **5b** in the absence of a dc field and (d) **5b** in the presence of a dc field of 1 kOe. The solid lines are visual guides

4 and **5b** showed maxima at a frequency higher than 10 and 50 Hz, respectively, whereas **5a** had no maximum at any frequency above 1.9 K. As **5a** and **5b** were similar in molecular structure as revealed by X-ray crystallography, the maximum of the χ'' signals for **5a** at each frequency might exist below 1.9 K. A similar axial-ligand dependence was observed in $[Co(X)_2$-

Table 6. Values of U_{eff} and τ_0 of **4**, **5a**, and **5b** in the Crystalline State and Frozen Toluene Solution

complexes	sample conditions	U_{eff} [K]	τ_0 [s]	ref
4	crystalline state	30	6.9×10^{-9}	this work
5a	crystalline state	ND[a]	ND[a]	this work
	frozen toluene solution	27	2.3×10^{-8}	
5b	crystalline state	28 (35)[b]	1.8×10^{-7} (5.1×10^{-8})[b]	this work
	frozen toluene solution	48	3.7×10^{-8}	
$[Co(NCS)_2(\mathbf{4NOpy})_4]$	frozen MTHF solution	31	1.7×10^{-7}	10
$[Co(NCO)_2(\mathbf{4NOpy})_4]$	frozen MTHF solution	50	1.8×10^{-7}	9

[a] Not determined. [b] The values in parentheses are the ones in the presence of a dc field of 1 kOe.

(**4NOpy**)$_4$] (X = NCS$^-$ and NCO$^-$) in frozen solution (Table 6). Because each frequency at the peak-top temperature for χ''_{mol} signals is consistent with $1/\tau$, the kinetic activation energy, U_{eff}, for the reversal of the magnetism and the pre-exponential factor, τ_0, were estimated from the Arrhenius plot; $\tau = 1/2\pi\nu_{ac} = \tau_0 \exp(U_{eff}/k_BT)$. The values of $U_{eff} = 30$ and 28 K and $\tau_0 = 6.9 \times 10^{-9}$ and 1.8×10^{-7} s for **4** and **5b** were obtained using the peak-top temperature data above 10 and 50 Hz, respectively (Figure S7, Supporting Information).

When the χ''_{mol} vs T plot of **5b** was closely examined, the χ''_{mol} signals at each frequency seemed to have a second peak (shoulder) on the lower temperature side. Then, the dc field dependence of the χ'_{mol} and χ''_{mol} signals was investigated. In the $\chi'_{mol}T$ vs T and χ''_{mol} vs T plots in the presence of a dc field of 1 kOe (Figure 12d), the $\chi'_{mol}T$ values at the lower temperature reached nearly zero, whereas the main peaks of χ''_{mol} signals shifted to the higher temperature side and the second peaks (or shoulder) almost disappeared. The χ''_{mol} vs T plot of **5b** in the presence of a dc field of 1 kOe gave values of $U_{eff} = 35$ K and $\tau_0 = 5.1 \times 10^{-8}$ s. (Figure S7). The change of χ'_{mol} and χ''_{mol} signals in the presence of the dc field suggests that the magnetic relaxation, k_d, observed by ac magnetic susceptibility measurements might be affected by the relaxation, k_q, due to the spin quantum tunneling effect.[2c,26] Fast relaxation, k_q, was often observed in the case of the Co complex carrying organic spins with a small S value in the heterospin systems.[9,10]

The strong dependence on frequency of the χ'_{mol} and χ''_{mol} signals and the physically reasonable values of τ_0 suggest that **4**, **5a**, and **5b** function as an SMM rather than a spin glass.[27,28] To better understand the magnetic properties of heterospin SMM, a theoretical study of **5b** and the ac measurements of **5a** and **5b** in frozen solution were carried out.

(B-3) Theoretical Study for 5b. To analyze quantitatively the magnetic property of **5b** showing SMM behavior,the ligand-field theoretical model[14,29] was employed. In this cobalt heterospin system, the effective Hamiltonian is written as

$$\hat{H} = \Delta \cdot \left(\hat{L}_z^2 - \frac{1}{3}\hat{L}^2\right) - \frac{3}{2}k\lambda\hat{L}\cdot\hat{S}_0 - 2J\sum_{i=1}^{4}\hat{S}_0\cdot\hat{S}_i + \mu_B\left(-\frac{3}{2}k\hat{L} + g_e\sum_{i=0}^{4}\hat{S}_i\right)\cdot B \quad (1)$$

where Δ and $\hat{L}$ are the energy splitting between $^4A_{2g}$ and ^4E_g states and an effective angular momentum with a magnitude of $L = 1$, respectively, $\hat{S}_0$ and $\hat{S}_i$ ($i = 1-4$) are spin operators of the Co(II) ion ($S_0 = {}^3/_2$) and four radicals ($S_i = {}^1/_2$), μ_B and g_e are the Bohr magneton and the Landé g factor for free electron, respectively, and parameters k, λ, and J stand for the Stevens orbital reduction factor of Co(II), the spin−orbit coupling of Co(II), and the superexchange interaction between Co(II) and each radical, respectively. Equation 1 fitted both sets of experimental data for the plots of $\chi_{mol}T$ *vs*. T (Figure 10) and $M/N\mu_B$ vs H/T (Figure 11) simultaneously by nonlinear least-squares fitting based on a downhill simplex method.[30−32]

The optimized parameters thus obtained are $\Delta/k_B = -1360$ K, $\lambda/k_B = -276$ K, $k = 0.866$, and $J/k_B = 16$ K for **5b** and simulation curves calculated using these parameter sets are shown in Figures 10 and 11.

The energy level scheme corresponding to **5b** is shown in Figure 13, where energy eigen values E of the Hamiltonian (eq 1) are plotted by levels with respective degeneracy figures against the z-component of the total spin quantum number M_S. The lowest six levels form a parabolic barrier profile with a height of 49 K, partitioning the $M_S = +5/2$ and $-5/2$ states. Although such a system possessing not-fully quenched orbital angular momentum cannot be described by using a zero-field splitting parameter D characteristic of the conventional Abragam-

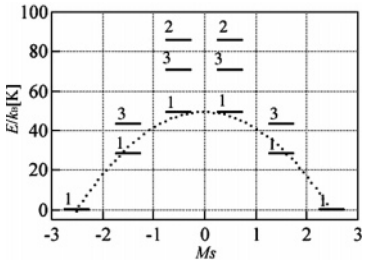

Figure 13. E/k_B vs M_s diagram for **5b** obtained from the optimized parameters. The broken curve is an eye-guide showing the energy-barrier profile for reversal of the resultant spin $S = {}^5/_2$.

(26) (a) Costes, J. P.; Dahan, F.; Wernsdorfer, W. *Inorg. Chem.* **2006**, *45*, 5−7. (b) Lu, Z. L.; Yuan, M.; Pan, F.; Gao, S.; Zhang, D. Q.; Zhu, D. B. *Inorg. Chem.* **2006**, *45*, 3538−3548.
(27) Mydosh, J. A. *Spin Glasses, An Experimental Introduction*; Taylor and Francis: London, 1993.
(28) (a) Gîrtu, M. A.; Wynn, C. M.; Fujita, W.; Awaga, K.; Epstein, A. *J. Phys. Rev. B* **2000**, *61*, 4117−4130. (b) Sellers, S. P.; Korte, B. J.; Fitzgerald, J. P.; Reiff, W. M.; Yee, G. *J. Am. Chem. Soc.* **1998**, *120*, 4662−4670. (c) Greedan, J. E.; Raju, N. P.; Maignan, A.; Simon, C.; Pedersen, J. S.; Niraimathi, A. M.; Gmelin, E.; Subramanian, M. A. *Phys. Rev. B* **1996**, *54*, 7189−7200.
(29) (a) Herrera, J, M.; Bleuzen, A.; Dromzée, Y.; Julve, M.; Lloret, F.; Verdaguer, M. *Inorg. Chem.* **2003**, *42*, 7052−7059. (b) Sakiyama, H.; Ito, R.; Kumagai, H.; Inoue, K.; Sakamoto, M.; Nishida, Y.; Yamasaki, M. *Eur. J. Inorg. Chem.* **2001**, 2027−2032. (c) Palii, A. V.; Tsukerblat, B. S.; Coronado, E.; Clemente-Juan, J. M.; Borra's-Almenar, J. J. *Inorg. Chem.* **2003**, *42*, 2455−2458. (d) Palii, A. V.; Ostrovsky, S. M.; Klokishner, S. I.; Reu, O. S.; Sun, Z.-M.; Prosvirin, A. V.; Zhao, H.-H.; Mao, J.-G.; Dunbar, K. R. *J. Phys. Chem. A* **2006**, *110*, 14003−14012. (e) Ostrovsky, S. M.; Falk, K.; Pelikan, J.; Brown, D. A.; Tomkowicz, Z.; Haase, W. *Inorg. Chem.* **2006**, *45*, 688−694. (f) Maspoch, D.; Domingo, N.; Ruiz-Molina, D.; Wurst, K.; Hernndez, J. M.; Lloret, F.; Tejada, J.; Rovira, C.; Veciana, J. *Inorg. Chem.* **2007**, *46*, 1627−1633.
(30) Nelder, J. A.; Mead, R. *Comput. J.* **1965**, *7*, 308−313.
(31) Parkinson J. M.; Hutchinson, D. In *Numerical Methods for Non-linear Optimization*; Lootsma, F. A., Ed.; Academic Press: London, 1972; pp 115−135.
(32) Press, W. H.; Teukolsky, S. A.; Vetterling, W. T.; Flannery, B. P. *Numerical Recipes*; Cambridge University Press: Cambridge, 1986.

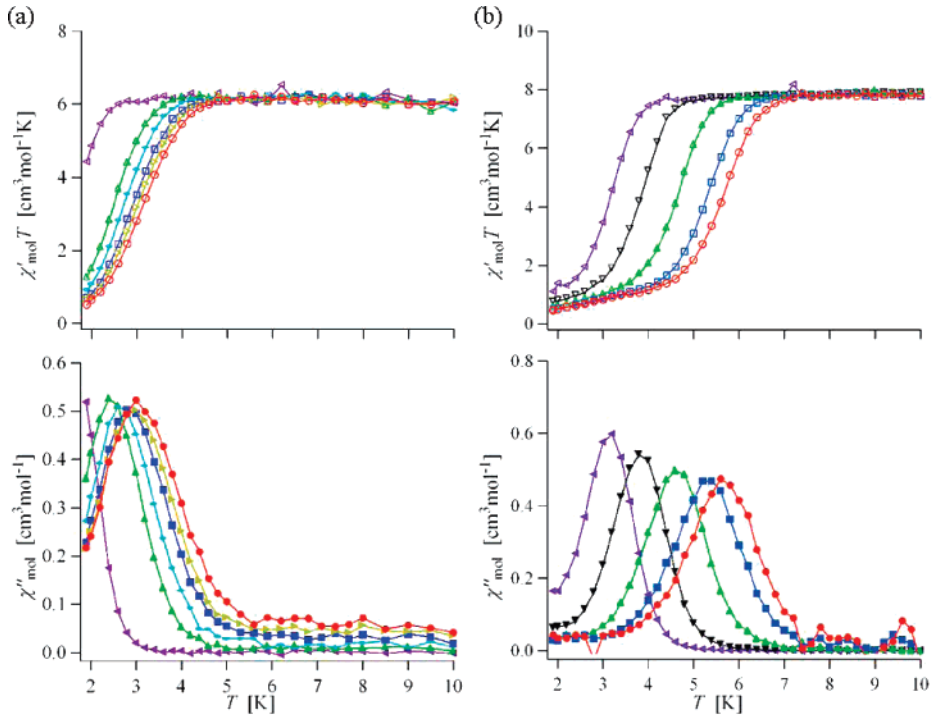

Figure 14. Plots of $\chi'_{mol}T$ vs T (upper) and χ''_{mol} vs T (lower) for the toluene solution samples of (a) **5a** and (b) **5b**. The solid lines are visual guides.

Pryce spin Hamiltonian, it was found that there exists another zero-field splitting in the ground spin manifold, which contributes to the thermodynamic activation barrier (U) for the reversal of the molecular spin. It should be noted here that the picture of the resultant molecular spin of $S = {}^5/_2$ has a certain relevance in the low-energy region of the energy level scheme. This resultant spin value is obtained if it is assumed that a high spin cobalt ion has a Kramers doublet ground state[29] with effective $S' = {}^1/_2$ and ferromagnetically interacts with four surrounding radicals.

Because the thermodynamic activation barrier, U, obtained by the calculation is the thermal activation over the potential energy for the reversal of the spin and the effective activation barrier, U_{eff}, obtained from ac magnetic susceptibility measurements involves quantum tunneling, the difference in the values, $U = 49$ and $U_{eff} = 28$ K, may arise from a resonance quantum tunneling.[33,34] The zfs parameter D/k_B for **5b** was estimated to be -8.2 K from the equation $U = |D|\{S^2 - (1/2)^2\}$ for a complex with a half-integer spin by $U = 49$ K.

(B-4) Ac Magnetic Susceptibilities of 5a and 5b in Frozen Solution. The complexes **5a** and **5b** were dissolved in dry toluene and used as solution samples (10 and 5 mM, respectively). The solutions of both complexes in toluene were measured by Visible spectra in the range of 300−180 K, and it was confirmed that, in an equilibrium between the tetrahedral and the octahedral structure, they are mainly the tetrahedral structure at room temperature and are predominantly the octahedral structure at 180 K (Figure S8, Supporting Information). The magnetic property of **4** in the frozen solution could not be investigated, because it was insoluble in toluene and other appropriate organic solvents. The ac magnetic susceptibility measurements for the toluene solution samples of **5a** and **5b** were carried out under conditions similar to those for the crystalline samples. The plots of $\chi'_{mol}T$ vs T and χ''_{mol} vs T are shown in Figure 14.

The frozen solution samples of both complexes showed a frequency dependence of χ' and χ'' signals similar to the crystalline samples of the corresponding ones. In the $\chi'_{mol}T$ vs T plots for the frozen solution samples, the $\chi'_{mol}T$ values in the plateau region are 6.20 and 7.80 cm^{3}mol^{-1}K for **5a**

and **5b**, respectively, and are consistent with those for the pulverized samples, indicating that the molecular structure of the complexes formed in frozen solution are octahedral, the same as those in the crystalline state. In the χ''_{mol} vs T plots, the peak-top temperature at each frequency shifted to a higher temperature. Especially, complex **5a** clearly showed a maxima of χ'' signal at above 99.9 Hz, although the pulverized sample of **5a** showed no maximum under similar conditions. Their Arrhenius plots (Figure S7, Supporting Information) gave U_{eff} and τ_0 values of 27 and 48 K, and 2.3×10^{-8} and 3.7×10^{-8} s for **5a** and **5b**, respectively. Both values became large compared with those obtained in the crystalline state. The observed difference of U_{eff} values for **5b** in the crystalline state and in the frozen solution might be caused by small changes in the local environment around the cobalt ion such as a change of the dihedral angles between the basal plane and the pyridine rings. The effect of crystal packing in the crystalline state is considered to be released in solution. The U_{eff} and τ_0 values for **4**, **5a**, and **5b** in the crystalline state and

(33) (a) Friedman, J.; Sarachik, M.; Tejada, J.; Ziolo, R. *Phys. Rev. Lett.* **1996**, *76*, 3830−3833. (b) Thomas, L.; Lionti, F.; Ballou, R.; Gatteschi, D.; Sessoli, R.; Barbara, B. *Nature* **1996**, *383*, 145−147.
(34) (a) Soler, M.; Wernsdorfer, W.; Folting, K.; Pink, M.; Christou, G. *J. Am. Chem. Soc.* **2004**, *126*, 2156−2165. (b) Hendrickson, D. N.; Christou, G.; Ishimoto, H.; Yoo, J.; Brechin, E. K.; Yamaguchi, A.; Rumberger, E. M.; Aubin, S. M. J.; Sun, Z.; Aromi, G. *Polyhedron* **2001**, *20*, 1479−1488. (c) Aubin, S. M. J.; Dilley, N. R.; Wemple, M. W.; Maple, M. B.; Christau, G.; Hendrickson, D. N. *J. Am. Chem. Soc.* **1998**, *120*, 839−840.

frozen solution are summarized in Table 6 together with those for $[Co(NCS)_2(\mathbf{4NOpy})_4]$ and $[Co(NCO)_2(\mathbf{4NOpy})_4]$ in frozen solution.

The U_{eff} and τ_0 values for **5a** and **5b** in the frozen solution are well consistent with those for the corresponding complexes, $[Co(NCS)_2(\mathbf{4NOpy})_4]$ and $[Co(NCO)_2(\mathbf{4NOpy})_4]$, obtained under similar conditions.

Conclusion

Because the magnetic property for an SMM originates from one molecule, an SMM molecule is required to be magnetically isolated in the crystal. However, the 1:4 complexes, $[Co(NCO)_2(\mathbf{4NOpy})_4]$ and $[Co(NCS)_2(\mathbf{C1py})_4]$, exhibiting SMM behavior in frozen solution, have strong intermolecular magnetic interactions in the crystalline state. To modulate the crystal structure of the heterospin systems, this time, **4NOpy** was replaced with the new *N*-aryl-*N*-pyridylaminoxyl ligand. With the new ligand, it is possible to introduce substituents on the phenyl ring and to modulate the crystal structure after the complexation with cobalt(II) ion by changing the bulkiness, the number, and the position of the substituent(s). The spin distributions for new *N*-aryl-*N*-pyridylaminoxyl ligands were confirmed by the DFT calculation. The 1:4 complexes of cobalt(II) ions with *N*-aryl-*N*-pyridylaminoxyls, $[Co(NCS)_2(\mathbf{PhNOpy})_4]$ (**1**), $[Co(NCS)_2(\mathbf{MeOPhNOpy})_4]$ (**2**), $[Co(NCS)_2(\mathbf{\textit{tert}\text{-}BuPhNOpy})_4]$ (**3**), $[Co(NCS)_2(\mathbf{TPPNOpy})_4]$ (**4**), $[Co(NCS)_2(\mathbf{TBPNOpy})_4]$ (**5a**), and $[Co(NCO)_2(\mathbf{TBPNOpy})_4]$ (**5b**) were prepared and the relations between the crystal structure and the magnetic properties were investigated. The molecular structure of all five complexes revealed by X-ray crystallography was a similar compressed octahedra. However, the crystal structure strongly depended on the bulkiness, number, and position of the substituent. The spin centers in complexes **1**, **2**, and **3** had various short contacts within 4 Å with the neighboring molecules to form magnetically the 2D structures. The distance between the 2D planes increased in the order of **1**, **2**, and **3**, which was consistent with the order of bulkiness of the substituent at the 4-position of the phenyl ring. In the crystals of **5a** and **5b**, on the other hand, there were no significant short contacts between the aminoxyl centers and between the aminoxyl center and the α- and β carbons of the pyridine ring of the neighboring molecules. These differences in crystal structure for the five complexes appeared as unique magnetic behavior due to the local and the structural magnetic anisotropy. The 1:4 complexes behaved as an antiferromagnet with $T_N = 22$ K for **1**, as a weak antiferromagnet with $T_N = 2.9$ K and $H_{sp}(1.9) = 0.7$ kOe for **2**, and as a canted 2D antiferromagnet (a weak ferromagnet) showing a hysteresis loop with $H_c = 1.3$ kOe below $T_N = 4.7$ K for **3**. In contrast, complexes **4**, **5a**, and **5b**, having no intermolecular interaction, functioned as SMMs. Especially, **5b** having bulky *tert*-butyl groups at the 2, 4, and 6-position of the phenyl ring, was found to have a U_{eff} value for the reversal of the magnetism of 28 K in the crystalline state and 48 K in frozen solution.

In this study, we could control the magnetic properties of discrete cobalt complexes in a heterospin system by using crystal engineering and finally succeeded in demonstrating the magnetic behavior of monometallic SMM in the crystalline state.

Acknowledgment. S.K. acknowledges a scholarship by the Japan Society for the Promotion of Science (JSPS). This work was supported by a Grant-in-Aid for Scientific Research (B)-(2)(No.17350070) from the Ministry of Education, Science, Sports, and Culture, Japan, and by the "Nanotechnology Support Project" of the Ministry of Education, Culture, Sports, Science, and Technology (MEXT), Japan.

Supporting Information Available: X-ray crystallographic file for five complexes and **TPPNOpy** and **TBPNOPy**, the spin density distributions for five *N*-aryl-*N*-pyridylaminoxyls, and various structural and magnetism figures as mentioned in the text. This material is available free of charge via the Internet at http://pubs.acs.org.

JA0767579